JOURNAL OF GEOPHYSICAL RESEARCH, VOL. 101, NO. B10, PAGES 22,291–22,309, OCTOBER 10, 1996

Seismic structure of the upper mantle in a central Pacific corridor

James B. Gaherty and Thomas H. Jordan

Department of Earth, Atmospheric, and Planetary Sciences, Massachusetts Institute of Technology, Cambridge

Lind S. Gee

Seismographic Station, University of California, Berkeley

Abstract. The seismic structure of the Tonga–Hawaii corridor has been investigated by combining two data sets: Revenaugh and Jordan's reflectivity profile from *ScS* reverberations, which provides travel times to and impedance contrasts across the major mantle discontinuities, and 1500 new observations of frequency-dependent phase delays for the three-component *S*, *SS*, and *SSS* body waves and the R_1 and G_1 surface waves, which constrain the velocity structure within this layered framework. The shear waves turning in the upper mantle showed significant splitting of the *SH* and *SV* components, indicative of shallow polarization anisotropy. The data set was inverted in conjunction with attenuation and mineralogical constraints to obtain a complete spherically symmetric, radially anisotropic structure. The final model, PA5, is characterized by a high-velocity, anisotropic lid, bounded at 68 km depth by a large (negative) G discontinuity; a low-velocity, anisotropic layer below G, extending to a small L discontinuity at 166 km; an isotropic, steep-gradient region between 166 km and 415 km; and transition-zone discontinuities at 415, 507, and 651 km. The depth of the radial anisotropy in PA5 is shallower than in most previous studies based on surface waves and higher modes. The average value of radial shear anisotropy in the lid, +3.7%, is consistent with the magnitude expected from the spreading-controlled models of olivine orientation, while anisotropy in the low-velocity zone, which is required by our data set, could be induced either by paleostrains that took place near the ridge crest or by shearing in the asthenosphere as a result of present-day plate motions. On the basis of recent work by Hirth and Kohlstedt, we suggest that the G discontinuity is caused by a rapid increase in the water content of mantle minerals with depth, marking the fossilized lower boundary of the melt separation zone active during crust formation. The high-gradient zone between 200 and 400 km is a characteristic feature of convecting oceanic upper mantle and is probably controlled by a steady decrease in the homologous temperature over this depth interval. The average shear-velocity gradient in the transition zone is lower than in most previous seismic models, in better agreement with the predictions for a pyrolitic composition.

Introduction

From a seismological perspective, the Pacific Ocean basin is the best natural laboratory for studying the structure of the oceanic mantle because it is nearly surrounded by active earthquake source regions, including deep-focus zones, that frequently illuminate its interior with seismic waves. It has been the testbed for many innovative studies in structural seismology, including seminal work on the three-dimensional (3-D) variability [e.g., *Leeds et al.*, 1974; *Suetsugu and Nakanishi*, 1987], anisotropy [e.g., *Forsyth*, 1975a; *Regan and Anderson*, 1984; *Farra and Vinnik*, 1994], and discontinuity structure [e.g., *Revenaugh and Jordan*, 1987, 1989; *Vidale and Benz*, 1992] of the upper mantle. Most recently, global and regional 3-D tomography has begun to provide more detailed maps of the lateral heterogeneity in the Pacific mantle [e.g., *Woodhouse and Dziewonski*, 1984; *Montagner and Tanimoto*, 1991; *Zhang and Tanimoto*, 1993; *Su et al.*, 1994]. While such tomographic studies have yielded useful images of the major geographic features, their data sets and model parameterizations have thus far suffered from inadequate resolution of vertical structure, especially with regard to the location and amplitudes of high-gradient regions (usually approximated as discontinuities) and the distribution of seismic anisotropy. These deficiencies have been particularly acute in the upper mantle, where typical global 3-D models display far less variability than observed among regional 1-D models [*Nolet et al.*, 1994]. Discontinuities and anisotropy are structural features that have considerable diagnostic value in the continuing assessment of the upper mantle's properties and processes, including its composition, phase, temperature, and deformation history [e.g., *Hess*, 1964; *Ringwood*, 1975; *Bass and Anderson*, 1984; *Weidner*, 1985; *Revenaugh and Jordan*, 1991a,b,c; *Karato*, 1992].

In this study, we use a novel and powerful combination of data to investigate the radial anisotropic structure in a narrow corridor from the Tonga-Fiji seismic zone to seismographs on the island of Oahu, Hawaii (Figure 1). We start with the results of *Revenaugh and Jordan* [1991c], who stacked *ScS* reverberations to obtain whole-mantle reflectivity profiles for this and other corridors in the southwest Pacific and Australasia. For most individual corridors, including Tonga-Hawaii, they were able to detect, locate, and measure the amplitudes of all mantle discontinuities with reflectivity peaks greater than about 1%. We use this precise, layered framework of vertical travel times and impedance contrasts in our construction of a regional upper

Paper number 96JB01882.
0148-0227/96/96JB-01882$09.00

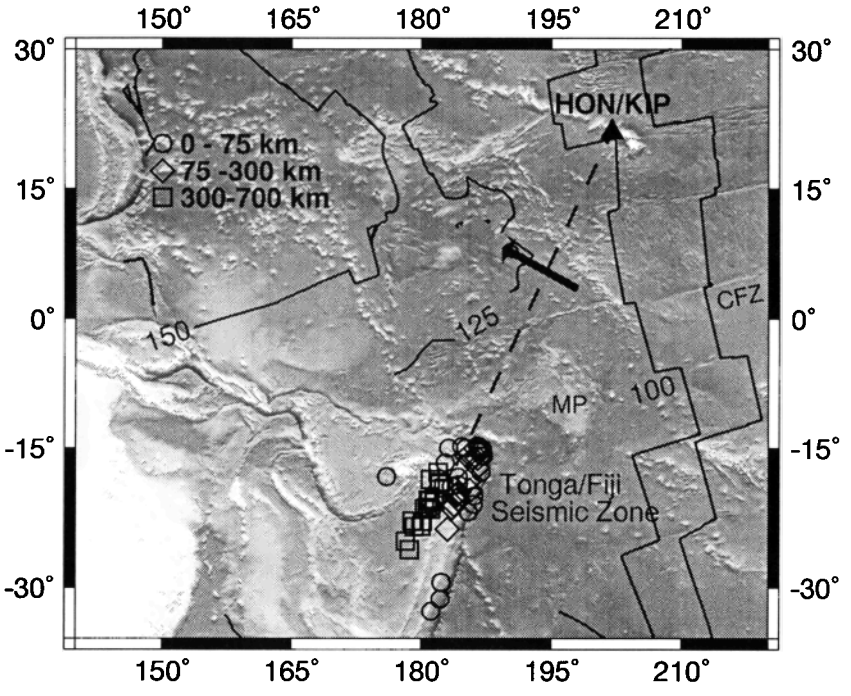

Figure 1. Mercator projection of the central Pacific showing the study corridor from the Tonga-Fiji seismic zone to the seismic stations HON and KIP on Oahu, Hawaii (triangle). Epicenters of the 55 Tonga-Fiji earthquakes used in this study are shown as open symbols (circles: shallow focus; diamonds: intermediate focus; squares: deep focus). The propagation path (dashed line) is oblique to the fossil spreading direction, as indicated by plate isochrons (black lines [from *Mueller et al.*, 1993], contoured in 25-Ma intervals) and by fracture-zone trends (e.g., Clipperton fracture zone (CFZ)), and it is roughly perpendicular to current plate motion relative to a hot-spot reference frame (black arrow [from *Gripp and Gordon*, 1990]). MP, Manihiki Plateau.

mantle structure. This framework is tied together by a new data set derived from the Tonga-Hawaii seismograms: 1500 frequency-dependent travel times measured from direct surface waves (R_1, G_1) and body phases (S), as well as from a variety of wave groups whose ray-theoretical decompositions contain the surface-reflected shear waves (e.g., *SS*, *sSS*, *SSS*).

At the epicentral distances and frequencies used in this study (Δ = 39°–58°; $f = \omega/2\pi$ = 10–45 millihertz (mHz)), the latter arrivals are essentially guided waves, arising from the complex interference of multiple refractions, reflections, and conversions from upper-mantle discontinuities. We account for these complexities in our waveform modeling, which is done by complete mode summation, and in our phase-delay inversions, which are based on *Gee and Jordan*'s [1992] theory of generalized seismological data functionals (GSDF). In the past, seismologists have typically applied different analysis techniques to the recordings of low-frequency guided waves on different seismographic components: ray-theoretical formulations in the case of transverse components of ground motion, which involve only horizontally polarized (*SH*) shear waves [e.g., *Grand and Helmberger*, 1984a, b], and mode-theoretical formulations for shear waves on the vertical and radial components, where the *P-SV* interactions are more complex [e.g., *Nolet*, 1975; *Lerner-Lam and Jordan*, 1983, 1987; *Zielhuis and Nolet*, 1994]. (An exception is the higher-mode study of *Cara and Lévêque* [1988], who derived dispersion curves for Pacific-crossing paths from both *P-SV* and *SH* wave trains. However, this frequency-wavenumber technique requires a large-aperture array for spatial filtering, severely limiting its applicability.) In the GSDF formulation of the structural inverse problem, the phase-delay spectra of all selected wave groups are measured by applying the same types of time- and frequency-localizing operations to the cross-correlations between synthetic wave groups (isolation filters) and the data seismograms. The partial derivatives of each phase delay are calculated with respect to all model parameters, including discontinuity depths, density, and anisotropic elastic parameters by formulae that account for the finite-bandwidth wave propagation and interference effects. GSDF thus provides a unified methodology for the analysis of complex wave groups on all three seismographic components.

Applying GSDF to the Tonga-Hawaii seismograms, we demonstrate that the *SH* and *P-SV* components of the surface and guided waves are significantly split by anisotropy situated in the uppermost mantle. This anisotropy is most likely related to the lattice-preferred orientation (LPO) of olivine in upper mantle peridotites caused by the horizontal shearing during plate formation and translation, which induces azimuthal asymmetry in the wave speeds [*Hess*, 1964; *Nicolas and Christensen*, 1987]. The observations presented here cannot resolve azimuthal variability, however, and we show that they can be satisfied by a transversely isotropic (radially anisotropic) model that incorporates no azimuthal variations. While such a model restricts our ability to address azimuthal anisotropy and its geodynamical significance, it does allow us to assess the distribution of anisotropy with depth and its relationship to discontinuities and other radial features of the mantle. The accuracy and uniqueness of the mapping between the actual anisotropy and our radial average using data from a single seismic corridor depends on the details of the olivine alignment, which are unknown. For example, if the LPO is largely horizontal but varies with respect to the propagation direction along the path, then the inferred radial model approximates an

azimuthal average of the local anisotropy [*Estey and Douglas*, 1986; *Jordan and Gaherty*, 1995]. If the LPO is coherently aligned at an oblique angle to the propagation direction, the resulting path-averaged anisotropy will be similar to the azimuthal average, but if coherent alignment coincides within ±20° of the propagation direction, the magnitude of the anisotropy obtained assuming transverse isotropy will underestimate the azimuthal average [*Lévêque and Cara*, 1983; *Maupin*, 1985]. As discussed below, our data, as well as other geological and seismological observations, indicate that the condition of parallel alignment is not likely to apply to the geometry of the central Pacific corridor investigated here.

We therefore invert the phase delays of the surface, guided, and body waves jointly with the *ScS* reverberation data for a path-averaged, layered, radially anisotropic model via an iterative, linearized scheme that perturbs the wave speeds, density, and discontinuity depths for each layer. As an aid to finding a geophysically plausible structure, we condition the inversion with a prior probability distribution on the model space that biases the estimate in favor of constraints derived from laboratory measurements and other seismic experiments relevant to the oceanic upper mantle. We also test a set of hypotheses that are alternatives to those imbedded in the model prior, with a specific focus on assessing the depth extent of seismic anisotropy in this part of the Pacific Ocean.

Tonga-Hawaii Corridor

The paths between earthquakes in the Tonga-Fiji seismic zone and the seismographic stations KIP and HON, both on Oahu, sample a relatively homogeneous corridor of old Pacific lithosphere (Figure 1). The crustal ages along this profile fall in a narrow range, 100-125 Ma [*Mueller et al.*, 1993], and its bathymetry is relatively uniform, with an average ocean depth of 5.1 km. The sediment thickness averages about 200 m [*Ludwig and Houtz*, 1979]. The corridor crosses the Line Islands and the eastern margin of the Darwin Rise, an area of prolific Cretaceous volcanism [*Menard*, 1984], but lies to the west of the disturbed upper mantle associated with the Pacific Superswell [*McNutt and Fischer*, 1987].

This relative homogeneity is reflected in seismic tomographic models [*Zhang and Tanimoto*, 1993; *Su et al.*, 1994; *Ekström and Dziewonski*, 1995]. Lateral velocity variations imaged in such models are small along the corridor, with higher shear velocities in the lid and lower shear velocities below the lid relative to the preliminary reference Earth model (PREM) of *Dziewonski and Anderson* [1981]. The corridor-averaged lower-mantle velocity is slow relative to PREM, and the root-mean-square (rms) variability increases substantially in region D" [*Su et al.*, 1994; *Ekström and Dziewonski*, 1995; *Garnero and Helmberger*, 1996].

The velocity of the Pacific plate in the hot-spot reference frame is roughly perpendicular to the corridor at a rate of 10.9 mm/yr [*Gripp and Gordon*, 1990]. However, the exact history of plate formation, of interest to us because the high strains associated with seafloor spreading largely determine the anisotropy of shallow mantle peridotites [*Ribe*, 1989, 1992], is difficult to discern, owing to the absence of magnetic reversals during the Cretaceous quiet period (~80-110 Ma) when much of the crust in this region was formed. The continuity of the major fracture zones across the Line Islands implies that the seafloor within the northern half of the corridor was formed at the Pacific-Farallon ridge in a geometry consistent with that preserved along the 75-Ma anomaly [*Menard*, 1967; *Joseph et al.*, 1987]. South of the equator, the bend in the 125-Ma contour and the presence of the rift-associated Manihiki Plateau imply a complex history of triple-junction spreading involving an ancient Phoenix plate [*Joseph et al.*, 1987]. The seafloor along the southern half of the corridor may have been formed on a NNW-SSE trending Pacific-Farallon or Phoenix-Farallon ridge, or along a WSW-ENE trending Pacific-Phoenix ridge. Either possibility implies that spreading-related fossil anisotropy is oblique to the corridor along much of its length.

Recent surface-wave and body-wave studies in this region have attempted to relate both the tectonic history of the plate, and the underlying mantle flow, to observed seismic anisotropy. Surface-wave observations include differential phase-velocity anomalies of Love and Rayleigh waves (polarization anisotropy) [*Cara and Lévêque*, 1988; *Nishimura and Forsyth*, 1989], azimuthal velocity variations of (primarily) Rayleigh waves [*Nishimura and Forsyth*, 1989; *Montagner and Tanimoto*, 1991], and surface-wave coupling [*Yu and Park*, 1994]. The first two indicate that the depth distribution and long-wavelength azimuthal variations of anisotropy are generally consistent with strain induced by both past and present plate motion, but the details of such structure are poorly resolved. The last is most sensitive to sharp gradients in anisotropy, and its presence implies that the anisotropy is spatially variable. Shear-wave splitting observed in body waves [*Farra and Vinnik*, 1994; *Su and Park*, 1994] provides localized estimates of azimuthal anisotropy, and they are also spatially variable. These estimates are sometimes correlated with either past or present plate motion, but they often disagree, and the sampling density of these waves is too low to precisely map the orientation and depth distribution of the azimuthal component in this region. Overall, the observations imply that multiple mechanisms, with various orientations and length scales, give rise to seismic anisotropy in Pacific upper mantle. Along our corridor, the likely alignment directions vary from oblique to perpendicular to the propagation direction. The radial anisotropy derived in this study can therefore be interpreted as a path average of this azimuthal variability, which should be close to a complete azimuthal average of the local anisotropy along the path [*Maupin*, 1985].

ScS Reverberations

Much of what is known about the details of mantle structure in this part of the Pacific has come from the study of *SH*-polarized *ScS* reverberations, which are very well excited at Oahu by dip-slip earthquakes in Tonga-Fiji. Reverberation phases are classified by their core-mantle boundary (CMB) reflection number, $n = 1, 2, \ldots$, and their reverberation order, $m = 0, 1, \ldots$, which is the number of times they reflect off one or more internal mantle discontinuities. We follow the conventions of *Revenaugh and Jordan* [1991b] in designating internal discontinuities above 400 km by a capital letter (M, Mohorovičić; H, Hales; G, Gutenberg; L, Lehmann) and transition-zone discontinuities by their nominal depths in kilometers, that is, 410, 520, 660, 710, and 900. The upper mantle refers to the region between M and 660, whereas the lower mantle refers to the region between 660 and the CMB.

The zeroth-order reverberations are the primary ScS_n and $sScS_n$ phases, which have long been used to study mantle attenuation [*Press*, 1956; *Kovach and Anderson*, 1964]. *Sipkin and Jordan* [1980b] applied a phase-equalization and stacking algorithm to 12 ScS_n phase pairs to estimate a path-averaged quality factor of $Q_{ScS} = 141 \pm 16$ for the Tonga-Hawaii corridor.

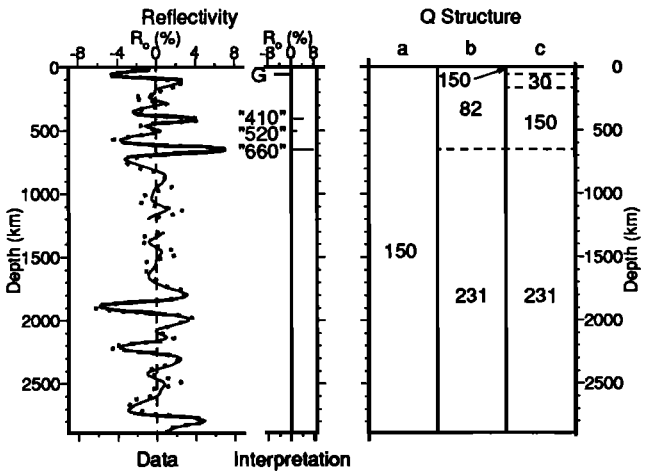

Figure 2. (left) Left side of panel compares the observed reflectivity profile for the Tonga-Hawaii corridor (dots) with a synthetic profile (solid line) obtained from the discrete discontinuity model shown in interpretation panel, from *Revenaugh and Jordan* [1991c]. The amplitudes and travel times associated with these discontinuities are the observed values listed in Table 1. (right) Shear Q structure for the Tonga-Hawaii corridor. (a) Average mantle Q from multiple-*ScS* observations [*Revenaugh and Jordan*, 1987]. (b) Q_{UM} and Q_{LM} from *ScS* reverberation observations [*Revenaugh and Jordan*, 1987]. (c) Q structure assumed for the modeling in this paper, based on the values shown in column b and our own surface and body wave observations for the Tonga-Hawaii corridor.

Revenaugh and Jordan [1987] expanded this data set to 26 ScS_n and $sScS_n$ phase pairs, obtaining $Q_{ScS} = 150 \pm 10$. They were also able to observe first-order reverberations from the 410 and 660 discontinuities as individual seismic phases. When referenced to the zeroth-order reflections, the first-order reverberations from a discontinuity d yield precise estimates of the vertical SV travel times from the surface to d and the reflectivity or impedance contrast across d,

$$t_d = \int_0^d v_{SV}^{-1}(z)\,dz \tag{1}$$

$$R_d = \frac{\rho v_{SV}(d^+) - \rho v_{SV}(d^-)}{\rho v_{SV}(d^+) + \rho v_{SV}(d^-)}. \tag{2}$$

Revenaugh and Jordan [1987] found the travel times of reverberations from the 660 discontinuity placed its apparent depth along the Tonga-Hawaii profile at 650 km, and an amplitude analysis combining the zeroth- and first-order reverberations yielded a reflectivity of $R_{660} = 0.080 \pm 0.004$, and quality factors of $Q_{UM} = 82 \pm 18$ and $Q_{LM} = 231 \pm 60$ for the upper mantle and lower mantle, respectively. We adopted these quality factors (which pertain to the 10-35 mHz band) as constraints on a simple forward modeling procedure to determine the attenuation model used in this study (Figure 2). They are lower than the global values of $Q_{UM}^{PREM} = 133$ and $Q_{LM}^{PREM} = 312$ calculated for the preliminary reference Earth model, which has an attenuation structure determined from low-frequency (3-10 mHz) free oscillations [*Dziewonski and Anderson*, 1981]. This discrepancy has been interpreted as a manifestation of the frequency dependence of mantle attenuation [*Sipkin and Jordan*, 1979].

Revenaugh and Jordan [1989, 1991a-d] developed a technique for stacking first-order *ScS* reverberations to obtain whole-mantle reflectivity profiles, which they applied to 18 seismic corridors. Their results for Tonga-Hawaii, reproduced in Figure 2 and Table 1, are used directly as data in our inversions. The reflectivity profile shows well-developed positive peaks from the 410 (4.6 ± 1.0%) and 660 (7.8 ± 1.0%) and a strong negative peak (–5.5 ± 2.0%) from a shallow G discontinuity; their apparent depths calculated from PREM and corrected for 3-D heterogeneity of *Woodhouse and Dziewonski* [1984] are 415, 653, and 59 km, respectively. The one-way differential travel time, $t_{660} - t_{410} = 45.5 \pm 1.0$ s, is slightly less than the global average (47 ± 1.5 s), suggesting that the transition-zone temperatures in this region are slightly higher [*Revenaugh and Jordan*, 1991b]. The shallow depth of G, which defines the top of the shear-wave low-velocity zone (LVZ), is consistent with inferences from surface-wave studies that properly account for polarization anisotropy in the uppermost mantle [*Regan and Anderson*, 1984].

A secondary but robust feature in the reflectivity profile is the distinctive loop between the 410 and 660 peaks introduced by the 520 discontinuity [*Revenaugh*, 1989; *Shearer*, 1990], which implies a small impedance contrast (2.1%) at an apparent depth of about 500 km. Notably absent is evidence for an H discontinuity near 60 km, which may be obscured by G [*Revenaugh and Jordan*, 1991c], and an L discontinuity near 220 km, which shows up in Australia as the sharp base of an anisotropic mechanical boundary layer [*Revenaugh and Jordan*, 1991c; *Gaherty and Jordan*, 1995].

The *ScS* reverberation data also allow us to address further the question of along-path heterogeneity. Although the path was chosen to sample what we assume is a relatively homogeneous part of the oceanic upper mantle, *Sipkin and Jordan* [1980a] observed that the differential travel times between multiple-*ScS*

Table 1. *ScS* Reverberation Data and Model Values for the Tonga-Hawaii Corridor

Discontinuity	Observed		Model PA2		Model PA5	
	t_d, s	R_d, %	t_d, s	R_d, %	t_d, s	R_d, %
M	1.7 ± 0.5	12.0 ± 5.0	2.3	18.4	2.1	16.4
G	12.0 ± 1.0	–5.5 ± 2.0	21.8	–3.4	14.2	–3.6
L	----	0.0 ± 1.0	41.1	0.8	36.8	0.4
410	91.1 ± 1.0	4.6 ± 1.0	89.7	4.5	91.8	3.9
520	107.7 ± 2.0	2.1 ± 1.5	----	0.0	109.7	1.3
660	136.6 ± 1.0	7.8 ± 1.0	141.2	7.1	136.5	8.0

Variable t_d is one-way, vertical SV travel time from the solid surface in seconds; R_d is the shear-wave impedance contrast at vertical incidence. Observations are from *Revenaugh and Jordan* [1991a, c].

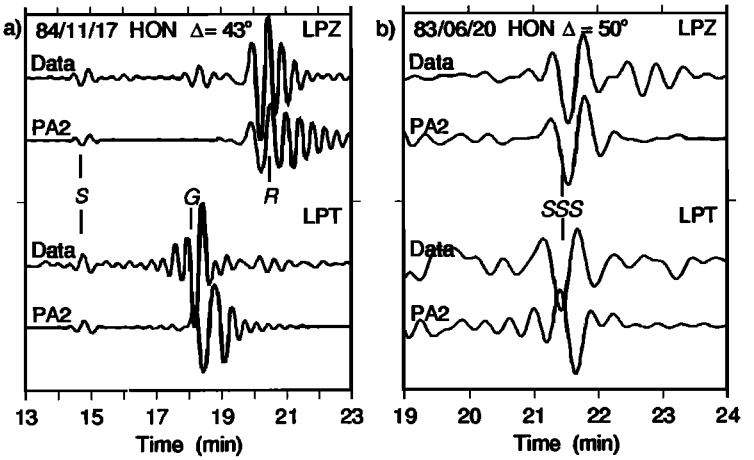

Figure 3. Examples of long-period seismograms showing direct evidence for polarization anisotropy. Top pair in each panel is vertical-component records; bottom pair is transverse components. First trace in each pair is the data seismogram; second trace is a synthetic for the isotropic model PA2. (a) Shallow-focus event (h = 10 km), with an S wave arriving at ~14.5 min, a (multimode) Love wave at ~18 min, and a Rayleigh wave at ~20 min. (b) Deep-focus event (h = 562 km); seismograms centered on an SSS arrival at ~21 min, with synthetics shifted to align the vertical-component waveforms.

phases show a large variation in ScS_n residuals (> 5 s in two-way travel time), which they interpreted as arising from a pattern of velocity anomalies in the upper mantle with north-south scale lengths of the order of 1000 km. Recent 2-D tomographic modeling of ScS and GSDF travel times [*Katzman et al.*, 1996] has confirmed the existence of this heterogeneity, but it has also shown that the model derived here (PA5) is a good path-averaged structure.

Frequency-Dependent Travel Times From Surface and Turning Waves

Frequency-dependent travel times have been measured from three-component, long-period seismograms at HON and KIP for an extensive set of direct Rayleigh (R_1) and Love (G_1) surface waves, direct S body waves, and a series of wave groups containing the surface-reflected shear waves, which include the phases SS, sSS, and SSS. To minimize unmodeled source effects, we limited our selection to Tonga-Fiji earthquakes of moderate size (M_w < 6.6) having well-determined Harvard centroid moment tensor (CMT) solutions [*Dziewonski et al.*, 1981]; 55 were chosen from 1983-1991, with hypocentral depths ranging from 10 to 663 km and epicentral distances from 39° to 58° (Figure 1). The horizontal-component seismograms were rotated into the radial and transverse directions, and all three components were low-passed with a zero-phase filter having a corner at 45 mHz.

Evidence of polarization anisotropy can be seen directly on the seismograms. Figure 3 compares the vertical and transverse seismograms observed from two events with synthetic seismograms computed for the isotropic model PA2 [*Lerner-Lam and Jordan*, 1987]. (All synthetic seismograms used in this paper were calculated by complete mode summation to 50 mHz, assuming the Harvard CMT and low-pass filtered like the data.) The initial Airy phase of the observed Rayleigh wave for the shallow-focus event (Figure 3a) is reasonably well matched by PA2 (which was derived from fundamental and higher-mode Rayleigh waves propagating across the northwest Pacific), while the observed Love wave clearly travels faster than the synthetic. The magnitude of the misfit cannot be rectified by perturbing the isotropic structure within reasonable bounds. Similarly, the SSS wave group from a deep-focus event (Figure 3b) shows clear evidence of shear-wave splitting, with SSS_H advanced by approximately 6 s relative to SSS_V. Splitting of this magnitude is typical of upper-mantle guided waves observed on other paths [*Gee and Jordan*, 1988; *Gaherty and Jordan*, 1995] and is diagnostic of anisotropy in the uppermost mantle.

Further evidence of this anisotropy may be seen on the vertical-component seismogram for the shallow-focus event, as a small arrival at about 18 min that is not well modeled by PA2 (Figure 3a). It is possible that this waveform represents Love-to-Rayleigh coupling from laterally variable azimuthal anisotropy in the central Pacific, as discussed by *Yu and Park* [1994]. In this distance range, however, this arrival closely coincides with the theoretical arrival time of SS_V, whose excitation in this case is very sensitive to source depth. By increasing the source depth from 10 to 20 km, we can generate SS_V on the vertical-component synthetics. Given this ambiguity we defer the interpretion of such anamolous waveforms and focus instead on the distinctive phase-delay anomalies associated with the polarization anisotropy.

GSDF Analysis

This procedure for measuring and inverting frequency-dependent travel times has its roots in the residual-dispersion methods pioneered by *Dziewonski et al.* [1972] and *Herrin and Goforth* [1977] and has theoretical affinities to the wave-equation travel-time inversion of *Luo and Schuster* [1991]. GSDF processing comprises six steps: (1) Synthesizing a target wave group to create a time-limited isolation filter. Although any convenient method for seismogram synthesis will do (e.g., asymptotic ray methods), we employ *Gee and Jordan's* [1992] mode-theoretic formulation, which obtains the isolation filter by summing traveling modes weighted according to the group and phase velocities of the target arrival. This synthesis procedure is exceptionally well suited for upper-mantle surface and guided waves, because it requires no high-frequency approximation and includes all wave interactions. (2) Cross-correlating the isolation filter with both the observed seismogram and the complete

synthetic seismogram. (3) Windowing the two broadband cross-correlagrams in the time domain. This time-localization operation reduces (but does not eliminate) the interference from other wave groups. (4) Filtering the windowed cross-correlagrams in a discrete set of narrow frequency bands $\{\omega_i \pm \sigma_i\}$. We typically center these filters at 5-mHz intervals across the frequency range from 10 to 45 mHz, which yields up to eight spectral estimates per isolation filter. This frequency-localization operation produces waveforms that under appropriate (and always enforceable) conditions can be approximated as Gaussian wavelets. (5) Fitting the windowed and filtered cross-correlagrams in the time domain with two five-parameter Gaussian wavelets. One of the five parameters is the (known) value of the bandwidth, σ_i; the other four can be written as a set of time-like quantities that include a phase delay, a group delay, and two equivalent amplitude parameters. On the synthetic cross-correlagram, nonzero values of these four parameters measure the interference between the isolation filter and other wave groups; subtracting these from the values estimated for the observed seismogram yields the interference-corrected data [*Gee and Jordan*, 1992, equations (9)-(12)]. (6) Correcting these data for windowing and filtering effects using equations (56)-(59) of *Gee and Jordan* [1992].

We limit our analysis to the differential phase delay, denoted $\delta\tau_p(\omega_i)$, which is our definition of a frequency-dependent travel time. Among the four generalized seismological data functionals recovered by the GSDF procedure, this observable is the most robust and useful in structural inverse problems. In particular, it is relatively straightforward to compute the Fréchet kernel $\mathbf{g}_p$ expressing its first-order sensitivity to a model perturbation $\delta\mathbf{m}$. For a spherically symmetric model,

$$\delta\tau_p(\omega_i) = \mathbf{g}_p(\omega_i)\cdot\delta\mathbf{m}. \qquad (3)$$

The inner product in (3) includes a sum over the discontinuities in $\mathbf{m}$, as well as an integral over depth. Under a set of approximations valid for the isolation filters used here, the Fréchet kernels can be written as a simple sum of the kernels for individual traveling modes:

$$\mathbf{g}_p(\omega_i) = \sum_{n=1}^{N} c_n \mathbf{g}_p^n(\omega_i). \qquad (4)$$

The coefficients $\{c_n\}$ depend on the isolation filter and the details of its interference with other wave groups on the seismogram, and they account for the excitation amplitude and phase of the source [*Gee and Jordan*, 1992, equations (73), (74), and (95)]. We have extended this formulation of the Fréchet kernels to include radially anisotropic, transversely isotropic media [*Gaherty*, 1995]. In this paper we utilize *Dziewonski and Anderson's* [1981] notation for the six medium parameters: mass density, $\rho(z)$; the speeds of horizontally and vertically propagating P waves, $v_{PH}(z)$ and $v_{PV}(z)$; the speed of horizontally propagating, transversely polarized shear waves, $v_{SH}(z)$; the speed of a shear wave propagating either horizontally with a vertical polarization or vertically with horizontal polarization (e.g., *ScS* reverberations), $v_{SV}(z)$; and a parameter that governs the variation of the wave speeds at oblique propagation angles, $\eta(z)$. Therefore $\delta\mathbf{m}$ comprises perturbations to these six functions of depth, as well as the perturbations to the depths of the internal mantle discontinuities.

Examples of GSDF Processing

Since this paper discusses the first full-fledged application of the GSDF methodology to a structural inverse problem, we illustrate some of its advantages with a few examples of waveform processing. Figure 4a displays the data, a full synthetic seismogram, and an isolation filter for a vertical-component *SSS* phase. The phase delays recovered by the GSDF procedure (Figure 4b) show that the *SSS* waveform is dispersed relative to the synthetic model; the low frequencies arrive approximately as predicted, whereas the higher frequencies arrive up to 8 s early. (A standard cross-correlation analysis yields only a single travel-time residual; in this case, approximately –6 s, which corresponds to the phase delay at ~35 mHz.) The Fréchet kernels relating these phase delays to model perturbations are also frequency dependent (Figure 4c). At low frequency, this *SSS* phase is sensitive primarily to the average *SV* velocity in the upper mantle, with two broad peaks near 100 and 300 km depth. At higher frequencies, the kernel becomes more oscillatory and more sharply peaked in the transition zone below 400 km depth, with the peak location eventually converging to its ray-theoretical bottoming depth of 480 km. Note that these phase delays do not depend on v_{SH}. They are sensitive, however, to the other model parameters, whose kernels are not plotted here.

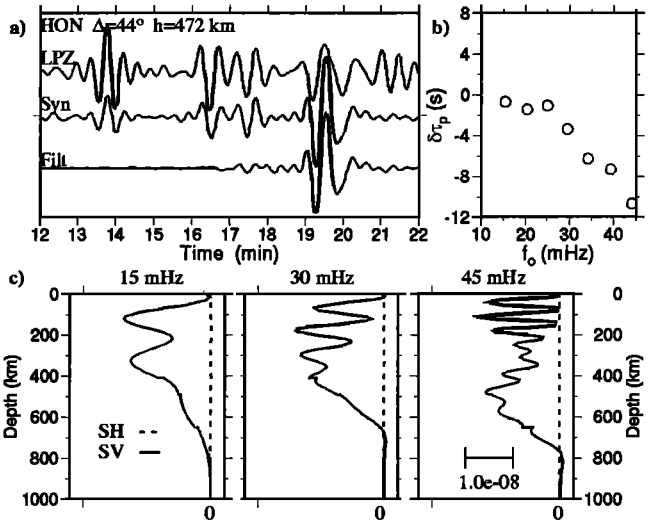

Figure 4. Example of the generalized seismological data functional (GSDF) processing, as discussed in the text. (a) (top) Observed, (middle) full synthetic, and (bottom) isolation filter seismograms for vertical-component data from a deep-focus event (h = 472 km). Observed phases are S (13.5 min), sS (16 min), SS (17 min), and SSS (19 min). The isolation filter is for SSS, constructed by summing spheroidal mantle modes with group velocities of 4.20 ± 0.1 km/s. (b) SSS phase delays $\delta\tau_p$ as a function of frequency, relative to the starting model. (c) Three sets of Fréchet kernels as a function of depth; the kernels relative to the two shear velocities for 15, 30, and 45 mHz are shown for this example. Solid line is the v_{SV} kernel, and dashed line is for v_{SH}.

The full power of GSDF analysis is illustrated by two versions of its application to the same multimode oceanic Love wave from a shallow-focus earthquake (Figures 5 and 6). Love waves provide critical information about anisotropic structure, but the lid/LVZ structure in oceanic regions results in very strong interference between the fundamental and higher modes, making traditional (single-mode) dispersion measurements difficult, especially along short propagation paths [*Thatcher and Brune*, 1969; *Forsyth*, 1975b; *Schlue and Knopoff*, 1977]. The isolation filter in Figure 5 (Filt1), obtained by integrating just the fundamental-mode branch, is a poor representation of the Love

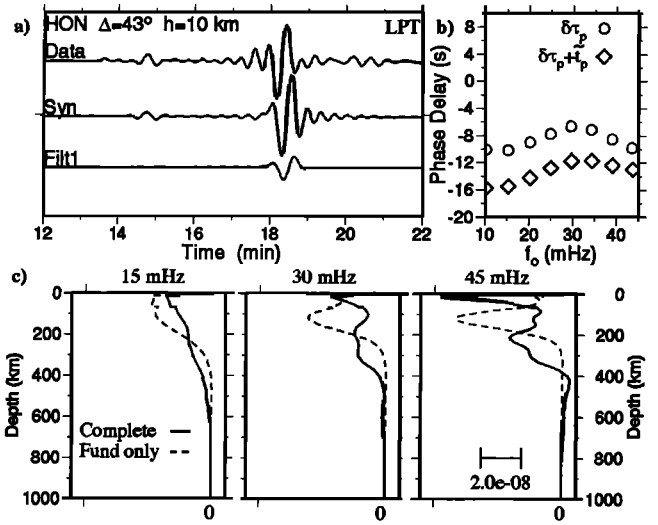

Figure 5. Example of the ability of GSDF to account for interference of complex waveforms. (a) (top) Observed, (middle) full synthetic, and (bottom) isolation filter synthetics for transverse-component data from a shallow-focus (h = 10 km) event. The S wave arrives at ~14.5 min, the multimode Love wave arrives at ~18 min. The isolation filter (Filt1) is constructed by summing only the fundamental-mode branch, and thus it does not include higher mode contributions and is a poor match to the full synthetic Love wave. (b) Initial phase-delay estimates $\delta\tau_p+\tilde{t}_p$, and final phase delays $\delta\tau_p$, as a function of frequency. The $\delta\tau_p$ have been corrected by up to 6 s by removing the interference term $\tilde{t}_p$. (c) Fréchet derivative kernels for v_{SH} (solid line) that are used to invert the $\delta\tau_p$ observations. The dashed line represents the kernels that would be used if the Love wave were assumed to be fundamental mode only (i.e., the interference corrections were not applied).

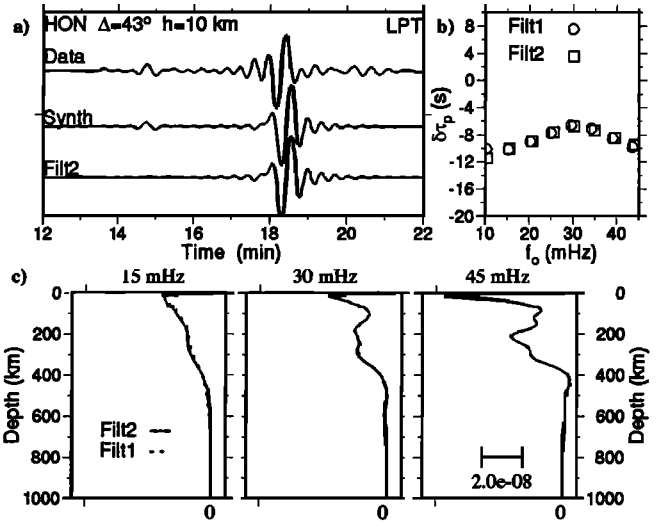

Figure 6. (a) Same data and full synthetic as Figure 5a, but with a new isolation filter (Filt2) constructed by summing all mantle modes with group velocities 4.34 ± 0.2 km/s. This filter represents an excellent match to the full synthetic Love wave, and interference corrections are negligible. (b) Final phase delays $\delta\tau_p$ for both Filt2 and Filt1 from Figure 5b. (c) The v_{SH} Fréchet derivative kernels for Filt2 and Filt1. The nearly identical behavior of the phase delays and kernels for these two filters demonstrates the robustness of the GSDF procedure.

waveform, which also contains significant energy from the first three overtones, whereas the one in Figure 6 (Filt2), constructed from all modes in the group-velocity window from 4.14 to 4.54 km/s, describes the waveform very well. The GSDF procedure yields the same results using either isolation filter. The interference corrections, obtained from the isolation-filter/full-synthetic cross-correlagram, are large and frequency dependent in the case of Filt1 (3-6 s, Figure 5b) but negligible for Filt2 (< 0.7 s), yet the interference-corrected phase delays are essentially identical (Figure 6b), except at 10 mHz, the very lowest end of the frequency band, where they differ by a little over a second. Moreover, the Fréchet kernels for both isolation filters overlay almost exactly (Figure 6c), although neither resembles the fundamental-mode kernel, especially at the higher end of the frequency band (Figure 5c). At 45 mHz, for example, the correct Fréchet kernel has a minimum where the fundamental-mode kernel has a maximum. Similar results are obtained using isolation filters corresponding to just the first or second overtone. This example demonstrates the robustness of the GSDF analysis to the choice of the isolation filter and its effectiveness in extracting precise and unambiguous structural information from the seismogram.

Data Summary

We selected 233 waveforms from the 55 Tonga-Fiji earthquakes, generated their isolation filters by weighted mode summation, and used GSDF processing to extract 1497 frequency-dependent travel times. We generally rejected waveforms which had low signal-noise ratio or were poorly matched by the synthetics (often indicative of errors in the source parameters or strong multipathing). All travel times were corrected for ellipticity, receiver, and source anomalies, which were calculated by averaging the tangential and vertical broadband S-wave delays for each event.

Figure 7 summarizes the travel-time residuals at 5-mHz intervals relative to the isotropic starting model PA2. Here each summary time is the mean over all distances and depths of all residuals classified in each of the following eight nominal wave categories: the SH surface wave G_1, guided waves SSS_H and SS_H, and body wave S_H from the transverse components (circles), and their P-SV equivalents, R_1, SSS_V, SS_V, and S_V, obtained by averaging over residuals from both the vertical and radial components (squares). This graphical representation of the data is admittedly rather crude, because it does not display variations observed in the residuals at different distances and hypocentral depths nor does it account for the variety of waves lumped into each data type. For example, waveforms from deep-focus events that have been classified as SSS often include the sSS phase, owing to the proximity of the sSS/SSS critical point. The GSDF travel times and kernels for such waveforms accurately incorporate the contributions of both phases.

The key features of the data set can nevertheless be recognized in Figure 7, and a feel for what they imply about mantle structure can be gleaned from examples of the Fréchet kernels for each of the eight wave types displayed in Figures 8 and 9. Differences between the R_1 and G_1 residuals are everywhere positive and reach 25 s near the low end of the frequency band. This is an example of the ubiquitous Love-Rayleigh (LR) discrepancy [*Anderson*, 1961; *McEvilly*, 1964; *Anderson and Dziewonski*, 1982]. It is indicative of polarization anisotropy of the normal type, that is, where $v_{SH} > v_{SV}$ and $v_{PH} > v_{PV}$. The Love waves are not strongly dispersed relative to PA2, but their mean is about 17 s faster, requiring v_{SH} in the lid and LVZ to be significantly

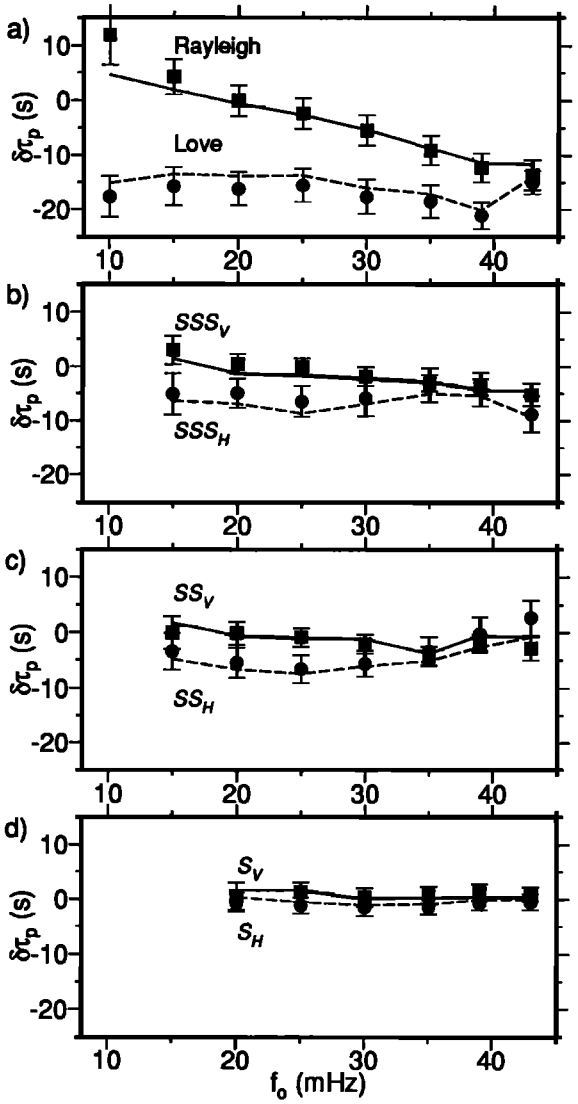

Figure 7. Summary of the frequency-dependent travel time data. Phase delays are categorized by phase type (surface wave, *SSS*, *SS*, or *S*), separated into tangential (*SH*, circles) or radial/vertical (*SV*, squares) observations, and averaged in each frequency band. Symbols represent the residuals relative to PA2, while the lines represent the predicted fit of model PA5 to these data. Dispersion relative to PA2 is indicated by a frequency-dependent trend, while evidence of anisotropy can be observed as a separation of the *SH* and *SV* observations for a given phase type: (a) Love and Rayleigh waves; (b) *SSS* and *sSS* waves; (c) *SS* waves; and (d) *S* waves. Error bars are determined by a weighted average of estimated a priori errors.

higher than the (isotropic) PA2 average. The strong negative slope in the R_1 residuals, on the other hand, favors values of v_{SV} similar to PA2 values, but a substantially thinner lid. A thin lid is also required by the *ScS* reverberation travel time from the G discontinuity (Table 1). Shear-wave splitting of the *SSS* and *SS* wavegroups is smaller than the LR discrepancy (≤ 8 s and 4 s, respectively), owing to their greater depth of penetration, and it also decreases with frequency. Since the low-frequency kernels of these guided waves are more concentrated in the shallow mantle than their high-frequency kernels, this frequency dependence limits the depth extent of the anisotropy. The *S* waves, which have high-frequency kernels that peak near their ray-theoretical turning depths (~1000 km), show little evidence of splitting or relative dispersion, requiring the anisotropy to be small in the transition zone and lower mantle.

Assuming an LPO origin of upper-mantle anisotropy, the observations imply an olivine *a*-axis alignment that is predominantly horizontal and not coherently parallel to the propagation path [*Maupin*, 1985; *Cara and Lévêque*, 1988], consistent with the inferences we have drawn from the geological and prior seismological data. This consistency further justifies using a transversely isotropic model for determining the depth distribution of anisotropy.

As emphasized by *Anderson and Dziewonski* [1982] and *Regan and Anderson* [1984], Rayleigh-wave travel times are sensitive to density, *P* velocities, and η, and the kernels for the other *SV* phases in Figures 8 and 9 show a similar dependence. In particular, their times all show a negative sensitivity to v_{PV} and a positive sensitivity to η. The sensitivity to v_{PH} is also positive, except near the surface. On the other hand, the *SV* times do not depend on v_{SH}, whereas the *SH* times are (negatively) sensitive to v_{SV}. Such behavior reinforces the importance of inverting for a fully radially anisotropic structure.

Inversion

The inversion was initiated with a starting model $\mathbf{m}_0$, chosen to be the isotropic PA2 structure of *Lerner-Lam and Jordan* [1987]. PA2 is parameterized in terms of a discrete set of layers with linear gradients bounded by sharp discontinuities corresponding to M, G, L, and the two major transition-zone discontinuities. We retained this basic parameterization throughout the inversion, except that we allowed a new discontinuity to develop in the transition zone in order to satisfy the *ScS* reverberation data for the 520-km discontinuity. Because an L discontinuity is not observed in the reflectivity profile for Tonga-Hawaii, we included $R_L = 0 \pm 1\%$ as a data point. A four-layer attenuation structure was constructed to match the *ScS* reverberation data and surface-wave amplitudes for this path, with layers separated by the G, L, and 660 discontinuities (Figure 2). The depths of these and all other discontinuities were allowed to vary during the inversions, but the four attenuation quality factors were held fixed. We accounted for the attenuative dispersion by assuming the layer *Q* values were frequency-independent [*Liu et al.*, 1976], which is a good approximation across the frequency band of the observations [*Sipkin and Jordan*, 1979]. We calculated the elastic parameters in the models at a reference frequency of 35 mHz.

The inversion sequence was carried through three iterations. In the *k*th iteration the difference between the true earth model $\mathbf{m}$ and the estimate $\mathbf{m}_{k-1}$ was assumed to satisfy the linearized system $\mathbf{A}_{k-1}\,\delta\mathbf{m} + \mathbf{n} = \delta\mathbf{d}_{k-1}$, where $\delta\mathbf{d}_{k-1}$ is the N-dimensional data-residual vector and $\mathbf{A}_{k-1}$ is the $N \times M$ matrix of partial derivatives computed for $\mathbf{m}_{k-1}$. The partials were calculated using ray theory and plane-wave reflection coefficients for the 11 *ScS* reverberation data and GSDF theory for the 1497 frequency-dependent travel times. In the latter case we integrated the Fréchet kernels in (4) over layers to obtain the partial derivatives of the data with respect to the layer slopes and intercepts. The data-error vector $\mathbf{n}$ was assumed to have zero mean, $\langle\mathbf{n}\rangle = 0$, and a diagonal covariance matrix $\mathbf{C}_{nn} = \langle\mathbf{n}\mathbf{n}^T\rangle = \mathrm{diag}[\sigma_1^2, \sigma_2^2, \ldots, \sigma_N^2]$. The standard deviations assigned to the *ScS* reverberation data depended primarily on the strength of the reflector, with σ_{R_d} and σ_{t_d} ranging from 0.005 and 1 s for the

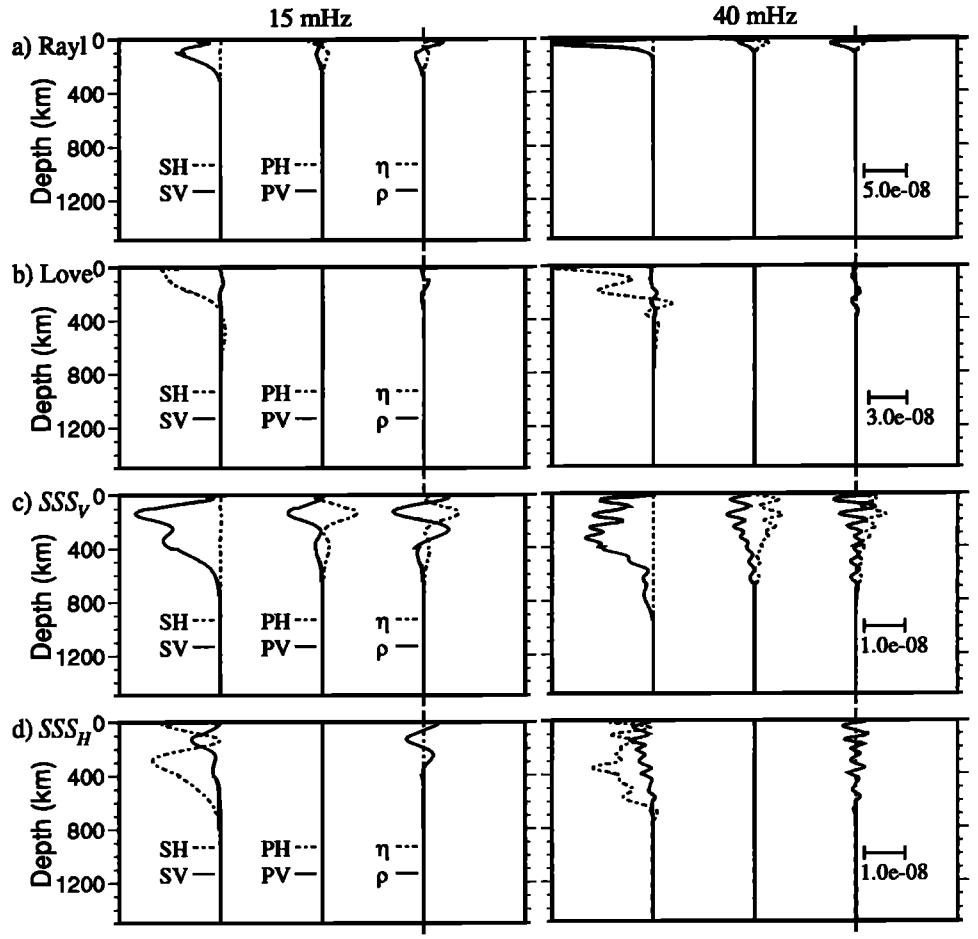

Figure 8. Fréchet derivative kernels for examples of different phase types. (a) Rayleigh-wave kernels and (b) Love-wave kernels, both for an event at $h = 10$ km. (c) Vertical-component and (d) tangential-component kernels for an *SSS* wave from an event at $h = 419$ km. Shown for each phase are two frames with (left) low frequency kernels (15 mHz) and (right) high frequency kernels (40 mHz). Within each frame, three pairs of kernels are shown: (left) shear kernels; (middle) compressional kernels; and (right) η and density kernels. P and η kernels for tangential-component phases are identically zero. Relative scales are maintained for each phase, with a scale on the far right in units of s km^{-3} x^{-1}, where x is the unit of the perturbation. The η kernel is also scaled by a factor of 4000 to facilitate plotting with density. Reference model is isotropic PA2.

bright 660-km and 410-km discontinuities to 0.01 and 2 s for the small 520-km discontinuity (Table 1). For the frequency-dependent travel times, the standard deviations ranged from 2 s for high-quality, high-frequency (40 mHz) times up to 10 s for low-quality, low-frequency (10 mHz) times. In the parameterization used for the final iterate (PA5), the model dimension was $M = 97$.

The perturbation $\delta\mathbf{m}$ was estimated by the nonlinear Gaussian-Bayesian procedure described by *Tarantola and Valette* [1982] and *Tarantola* [1987]. We imposed an a priori Gaussian probability distribution on $\delta\mathbf{m}$ having an expectation vector $\langle\delta\mathbf{m}\rangle = \overline{\mathbf{m}} - \mathbf{m}_{k-1}$ and a positive-definite covariance matrix $\langle\delta\mathbf{m}\delta\mathbf{m}^T\rangle = \mathbf{C}_{mm}$, and we calculated the estimate

$$\delta\mathbf{m}_k = [\mathbf{A}_{k-1}^T \mathbf{C}_{nn}^{-1} \mathbf{A}_{k-1} + \mathbf{C}_{mm}^{-1}]^{-1} \cdot [\mathbf{A}_{k-1}^T \mathbf{C}_{nn}^{-1} \delta\mathbf{d}_{k-1} + \mathbf{C}_{mm}^{-1}(\overline{\mathbf{m}} - \mathbf{m}_{k-1})] \quad (5)$$

After each step, the model was evaluated by a complete remeasurement of the data using synthetic seismograms and isolation filters computed for the new model $\mathbf{m}_k = \mathbf{m}_{k-1} + \delta\mathbf{m}_k$.

Our prior knowledge of earth structure was specified by the M vector $\overline{\mathbf{m}}$ and the symmetric $M \times M$ matrix $\mathbf{C}_{mm}$. Several different types of information and assumptions were combined in the construction of these quantities. For example, at six discrete depths between 250 and 720 km we constrained the density ρ and bulk sound velocity $v_\phi = (v_P^2 - 4v_S^2/3)^{1/2}$ to satisfy the estimates obtained by *Ita and Stixrude* [1992] for a pyrolite mineralogy, assigning a standard error of ± 1% to each estimate (Figure 10). These parameters, which are complementary to our shear-wave-dominated data set, can be inferred with reasonable precision from laboratory observations; moreover, the choice of a pyrolite composition is not particularly restrictive, since the $v_\phi(z)$ and $\rho(z)$ profiles for most competing mineralogical models (e.g., high-aluminum piclogite) differ from pyrolite by less than the assigned errors [*Ita and Stixrude*, 1992]. We also assumed that the jumps in both v_ϕ and ρ were small (± 0.5%) at the G and L discontinuities. This requirement was loosened to ± 1% for ρ at the 520-km discontinuity, where a density increase of 0 to 2% is expected for the β–γ transition in $(Mg, Fe)_2SiO_4$

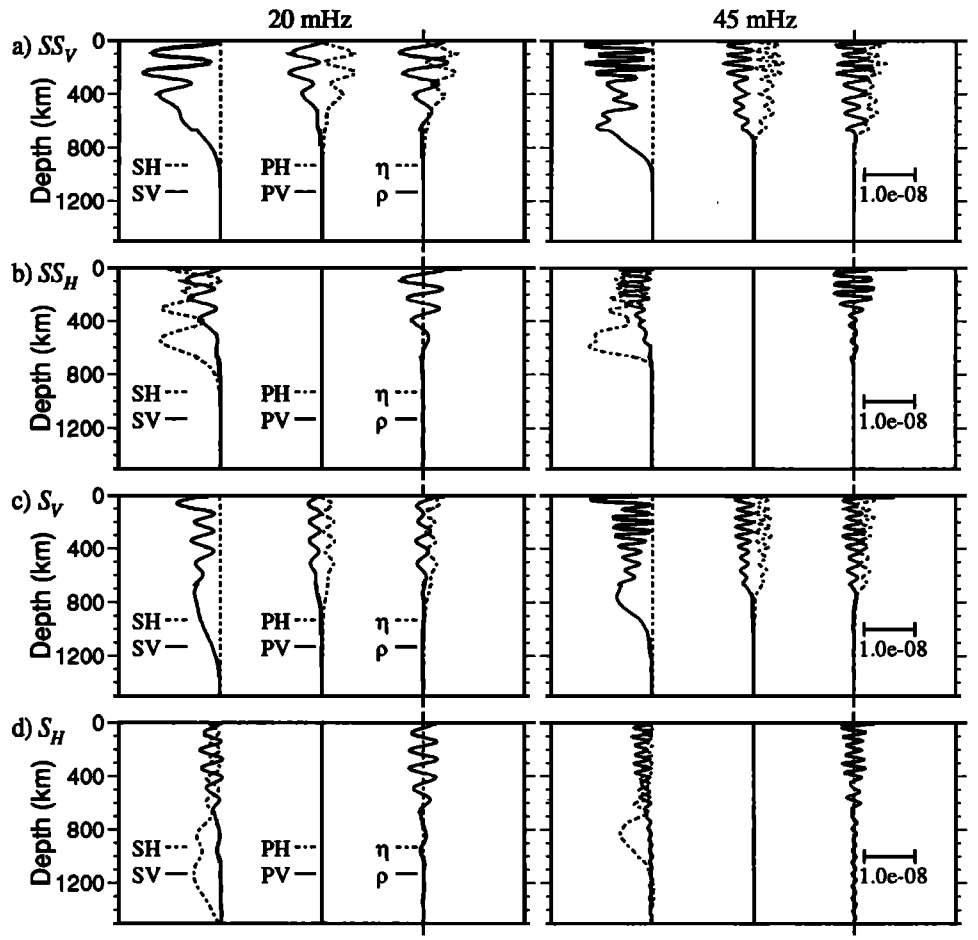

Figure 9. Fréchet derivative kernels for vertical- and tangential-component *SS* (a,b) and *S* (c,d). All kernels are shown at (left) 20 mHz and (right) 45 mHz. Otherwise, plotting is the same format as Figure 8. Note that while SS_V and S_V have little sensitivity to v_{SH}, SS_H and S_H have significant sensitivity to v_{SV} at shallow depths.

[*Ita and Stixrude*, 1992; *Rigden et al.*, 1991].

We built into the model prior three types of constraints on the amount of anisotropy. We assumed that below some depth z_{max}, which we varied in different inversions (described below), the mantle is isotropic, that is, $v_{PH} = v_{PV}$, $v_{SH} = v_{SV}$, and $\eta = 1$. In the anisotropic region above z_{max}, we assumed the anisotropy ratio for *P* waves, $\Delta v_P / \bar{v}_P = 2(v_{PH} - v_{PV})/(v_{PH} + v_{PV})$, is equal to that of *S* waves to within ± 2%, consistent with theoretical calculations for a pyrolite mineralogy [*Estey and Douglas*, 1986] as well as observations of mantle rocks [*Christensen*, 1984]. Finally, we constrained $\eta(z)$ in anisotropic layers to be close to those in PREM (± 5%), which also conforms to mineralogical expectations [*Nataf et al.*, 1986; *Montagner and Anderson*, 1989].

To complete the prior, we assumed that the shear velocities and all otherwise unconstrained model parameters had expected values equal to those in the PA2 starting model. These estimates were assigned large standard deviations (± 0.5 km/s for v_S, ± 20 km for discontinuity depths), except in the crust and shallowest portion of the mantle, where we had independent estimates from rock samples and shallow seismic refraction data [e.g., *Shearer and Orcutt*, 1986]. In the crust, for example, we took the prior uncertainties to be 0.1 km/s for wave speeds and 0.1 g/cm^3 for density.

Our preferred model for the Tonga-Hawaii corridor, PA5, is presented in Figure 11 and Table 2. The progression from PA2 to PA5 involved three complete iterations of the linearized inversion. In the first iteration, we reduced the sediment thickness from 1 to 0.2 km to match better the geological estimates for the corridor [*Ludwig and Houtz*, 1979], and we restricted the anisotropy to the seismic lid above the G discontinuity by setting $z_{max} = z_G$ in the model prior. The resulting perturbation accounted for some of the larger discrepancies between PA2 and the observations. To satisfy the *ScS* reverberation data in Table 1, the lid was thinned substantially, the 410 was deepened, the 660 was raised, and a 520 was introduced. The fit to the average surface-wave and body-wave phase delays was improved by thinning the lid and raising its shear velocities, and the splitting observed for these phases was accommodated by introducing radial anisotropy.

Significant residuals remained, however, including large negative residuals in the Love-wave phase delays that indicated the need for more anisotropy. In the next iteration, we conducted a series of experiments to investigate the depth extent of the anisotropy. We first reinverted the data set (remeasured using isolation filters calculated for the new reference model, PA3) retaining the constraint $z_{max} = z_G$, that is, under the hypothesis that the anisotropy is dominated by lattice preferred orientation frozen into a thin mechanical boundary layer (MBL), identified with the lid. We found that models of this type could not fit both the Love and Rayleigh waves. The problem is most evident in the Love waveforms, as illustrated in Figure 12; models with

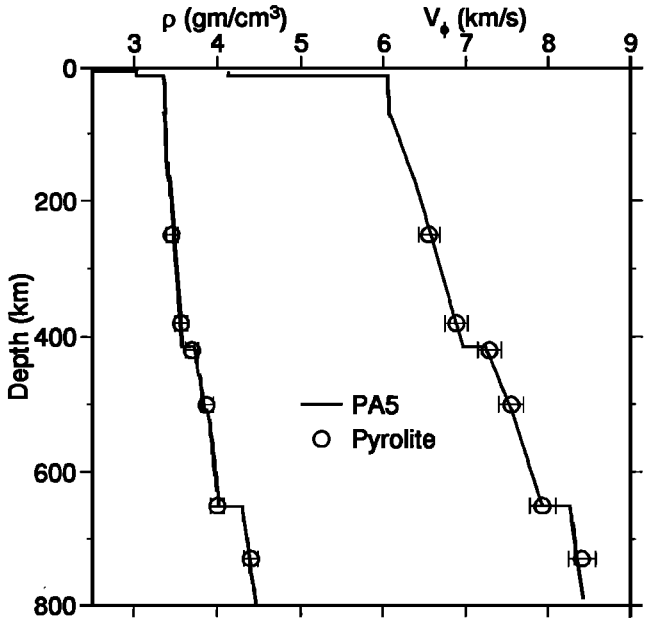

Figure 10. Values of density ρ and bulk sound velocity v_ϕ calculated by *Ita and Stixrude* [1992] for the pyrolite model (circles with error bars). These were used to construct prior distributions for ρ and v_ϕ in the inversion. The values calculated from resulting model PA5 (solid lines) are shown for comparison.

anisotropy restricted to the lid produce simple, impulsive groups, like the trace labeled A_{70}, whereas the data show a more complex, emergent waveform caused by a dephasing of the first three overtones with respect to the fundamental. (Note that the first two higher modes are larger than the fundamental.) To accomplish this dephasing, it was necessary to increase the *SH* velocity in the LVZ, which advances the 0th- and 1st-mode branches relative to the 2nd and 3rd. Anisotropy in the LVZ was thus required in order to maintain the *SV* contrast across the G discontinuity, as dictated by the *ScS* reverberation data.

We therefore relaxed the constraint on the depth extent of the anisotropy by setting $z_{max} = z_{410}$, which resulted in a model (PA4) with anisotropy extending throughout the LVZ. The anisotropy in the high-gradient zone (HGZ) between 200 and 400 km was small, however (~1% or less). Further experiments demonstrated that the velocity gradients in this region are well determined by both the *SH* and *SV* dispersion data, from which we concluded that the anisotropy of the HGZ must be minor. In the third and final iteration, we set $z_{max} = z_L$, the depth to the interface (internal to the LVZ) that defines the top of the HGZ. This depth is unconstrained by the *ScS* reverberation data, although the *SV* contrast across it was required to be small ($0 \pm 1\%$) to satisfy the lack of an L discontinuity peak in the reflectivity profile. The resulting model, PA5, provides a good overall fit to the data set (Table 1, Figure 7), yielding a variance reduction of over 80% relative to PA2. Anisotropy in the model extends to z_L = 166 km, which gives a good match to the Love waveforms not obtained by models with shallower anisotropy (Figure 12).

Observed seismograms are compared with the full mode-synthetic seismograms calculated for PA5 in Figure 13. These events were chosen solely because they represent a variety of source depths and distances with mechanisms that yield strong signals on both transverse and vertical components; hence they are truly representative of our complete data set. The overall match is quite good, especially considering that the misfits are

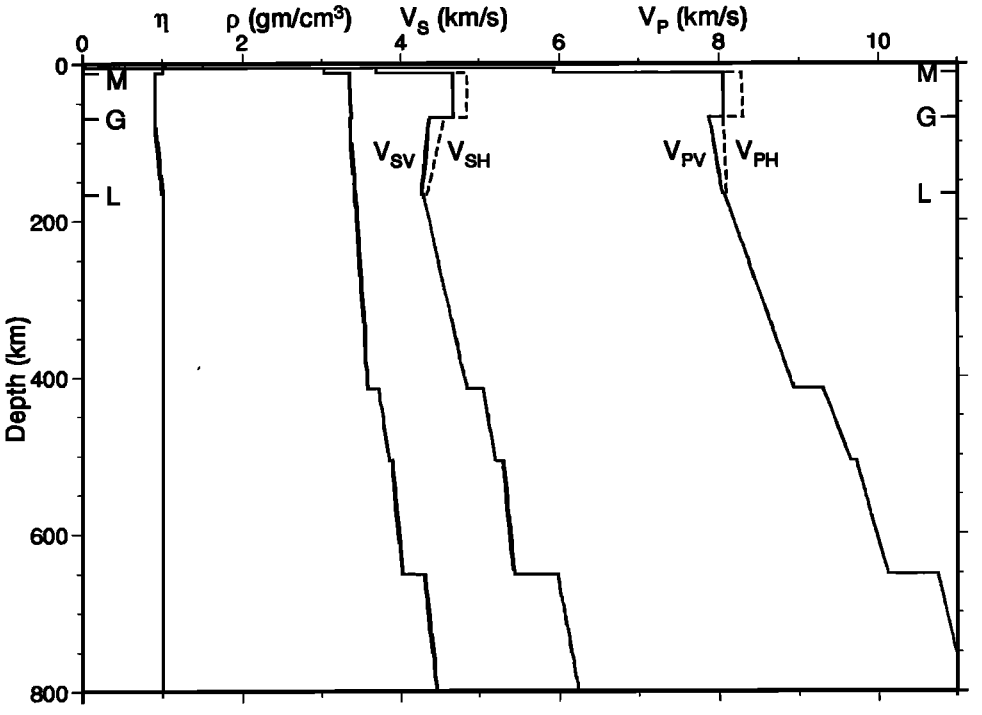

Figure 11. Model PA5. From left to right, η, density, shear velocities, and compressional velocities are plotted as a function of depth. The model is radially anisotropic through the lithosphere and the low-velocity zone, with v_{SH} and v_{PH} being higher than v_{SV} and v_{PV}, respectively. Below 800-km depth, the model is the same as the preliminary reference Earth model (PREM) at a reference frequency of 35 mHz.

Table 2. Model PA5

z, km	ρ, Mg/m^3	v_{SV}, km/s	v_{SH}, km/s	v_{PV}, km/s	v_{PH}, km/s	η
0.	1.03	0.00	0.00	1.50	1.50	1.00
5.	1.03	0.00	0.00	1.50	1.50	1.00
5.	1.50	0.92	0.92	2.01	2.01	1.00
5.2	1.50	0.92	0.92	2.01	2.01	1.00
5.2	3.03	3.68	3.68	5.93	5.93	1.00
12.	3.03	3.68	3.68	5.93	5.93	1.00
12.	3.34	4.65	4.84	8.04	8.27	0.90
68.	3.38	4.67	4.83	8.06	8.30	0.90
68.	3.35	4.37	4.56	7.88	8.05	0.90
166.	3.41	4.26	4.34	8.04	8.09	1.00
166.	3.42	4.29	4.29	8.06	8.06	1.00
415.	3.58	4.84	4.84	8.92	8.93	1.00
415.	3.71	5.04	5.04	9.29	9.29	1.00
507.	3.85	5.20	5.20	9.64	9.64	1.00
507.	3.88	5.28	5.28	9.71	9.71	1.00
651.	4.02	5.43	5.43	10.11	10.11	1.00
651.	4.29	5.97	5.97	10.76	10.76	1.00
791.	4.46	6.23	6.23	11.08	11.08	1.00
791.	4.46	6.23	6.23	11.08	11.08	1.00
801.	4.46	6.24	6.24	11.10	11.10	1.00

Model is calculated at a reference frequency of 35 mHz; it is identical to PREM below 801 km.

almost always associated with phases such as *sS*, *ScS*, and *sScS*, which show considerable variability caused by near-source and lower-mantle structure not modeled by PA5 [*Katzman et al.*, 1996].

Discussion

The formal standard errors in the model parameters are easily calculated from the a posteriori covariance matrix associated with (5), but these values tend to underestimate the actual uncertainties in structural inverse problems, which are often dominated by hidden biases in the data and assumptions underlying the model parameterization [*Woodhouse and Dziewonski*, 1984]. In the discussion that follows, our assessment of the structural features of PA5 therefore combines these posterior uncertainties with other measures, such as the structural variations associated with plausible modifications to the model prior, the sensitivity of the model parameters to possible bias in subsets of data, and the compatibility of PA5 with previous studies of oceanic upper-mantle structure, especially those based on data complementary to the set used here. In general, the model parameters best resolved directly by our seismic observations are the depths to the major discontinuities (M, G, 410, 660), the *SV* impedance contrasts across these discontinuities, and the *SH* and *SV* velocities in the layers above the 410. The precisions attached to the *P* velocities, density ρ, and anisotropy parameter η are much more sensitive to the assumptions built into the model prior, particularly the mineralogical constraints on v_ϕ and ρ. We thus focus our discussion on the shear-velocity structure. We note, however, that PA5 satisfies the constraints in Figure 10 without compromising the fit to the seismic data, which implies that the seismic data are consistent with these aspects of a pyrolite mineralogy.

Radial Anisotropy

The depth of anisotropy in PA5 is 166 km, shallower than in previous studies based on surface waves and higher modes, which range from 220 km [*Regan and Anderson*, 1984] to over 300 km [*Cara and Lévêque*, 1988; *Nishimura and Forsyth*, 1989]. This difference probably reflects the model parameterizations and minimization criteria more than any significant observational discrepancies. *Regan and Anderson* [1984] adopted a PREM-like structure with anisotropy extending to an L discontinuity fixed at 220 km, while the other two studies employed smooth parameterizations that permitted small amounts of anisotropy at greater depths. Between G and 410, PA5 has only two layers separated by a (small) L discontinuity, which delineates the base of the anisotropy. The formal error in the depth to L (±10 km) is considerably smaller than that estimated for the depth of anisotropy (±30 km), although in PA5 these depths are constrained to be identical. Additional inversion experiments using more layers indicated that the data marginally prefer a distribution of anisotropy that extends slightly deeper and an L that is smaller than in PA5. However, in all of these experiments, the large splitting observed for the surface waves combined with the smaller splitting of the reflected shear waves (Figure 7) constrained the integral of the anisotropy ratio $\Delta v_S / \bar{v}_S = 2(v_{SH} - v_{SV})/(v_{SH} + v_{SV})$ to be small (< 1%) between 200 km depth and the 410 discontinuity. Because these models contained more free parameters but did not significantly improve the fit to the data, we maintained the simpler parameterization of PA5.

The frequency-dependent travel times used in the PA5 inversion are integrals of a projection of the total (3-D) anisotropy onto the direction of wave propagation. Seismic refraction experiments and laboratory measurements on rock samples from ophiolites have demonstrated that the anisotropy in the lid is primarily due to lattice preferred orientation in olivine, with the fast *a* axis nearly horizontal and aligned with the initial seafloor spreading direction [*Nicolas and Christensen*, 1987]. On a hand-sample scale the peridotite anisotropy ranges from 3-8% in *P* waves and 3-6% in *S* waves [*Christensen*, 1984]. The projection of this fossilized anisotropy onto the propagation path is expected to yield radial anisotropy ratios $\Delta v_S / \bar{v}_S$ that are positive and large (up to 5%) for paths perpendicular or oblique

to the spreading direction, but small (and even negative) for paths parallel (within ±20°) to this direction [*Kawasaki and Kon'no*, 1984; *Maupin*, 1985]. Although the plate reconstructions for the southern part of the corridor are uncertain [*Joseph et al.*, 1987], the corridor axis probably has a mean orientation of about 50°-60° relative to the seafloor-spreading directions. The average value of $\Delta v_S / \bar{v}_S$ in the PA5 lid, +3.7%, is thus consistent with

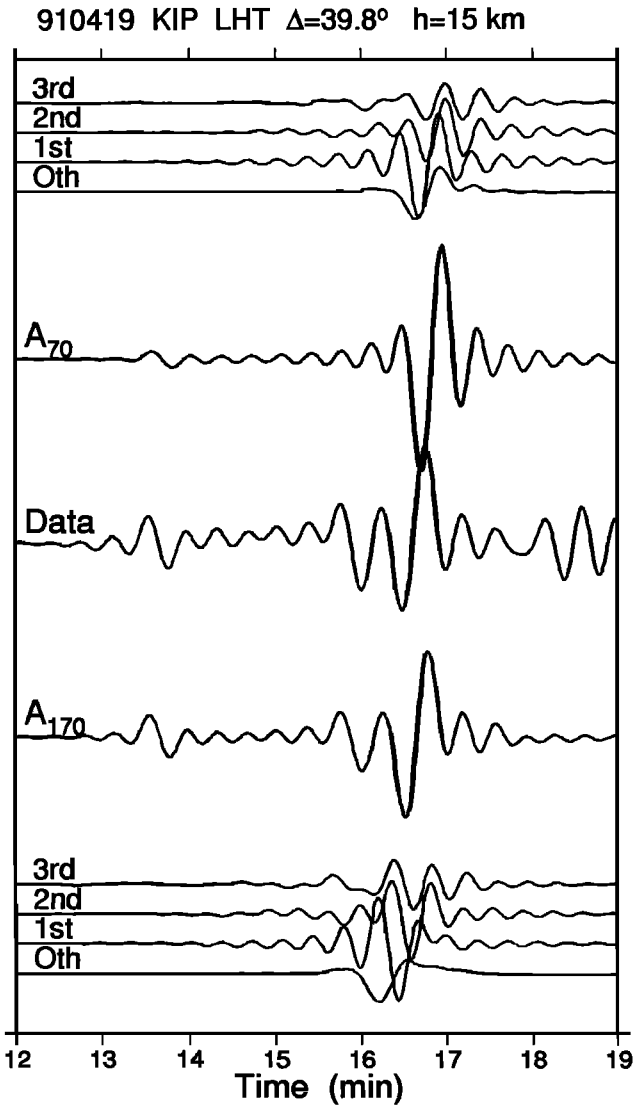

Figure 12. Seismograms showing a multimode Love wave that is diagnostic of high v_{SH} in the LVZ. The observed seismogram (center trace) is the transverse component recorded at KIP from a shallow-focus event. The direct *S* wave arrives at ~13.5 min and the emergent Love-wave group at ~16 min. The trace labeled A_{70} is a complete synthetic seismogram for an Earth model where anisotropy is restricted to the upper 70 km. Synthetics of the first four mode branches (0th-3rd) for A_{70} are displayed above the full synthetic. The trace labeled A_{170} is a complete synthetic for PA5, where the anisotropy extends into the LVZ. Synthetics of the first four mode branches (0th-3rd) for PA5 are displayed below the full synthetic. Comparision of the mode-branch synthetics for the two models demonstrates that the increased *SH* velocity in the LVZ in PA5 enhances and advances the 0th and 1st mode branches, thereby generating a complete synthetic with emergent, dispersed behavior similar to that observed in the data.

the magnitude expected from the spreading-controlled LPO models [e.g., *Kawasaki and Kon'no*, 1984]. This shear anisotropy is also comparable to the PREM global value and to azimuthally averaged regional models of the central and western Pacific [*Nishimura and Forsyth*, 1989], as well as that observed for the uppermost mantle beneath Australia [*Gaherty and Jordan*, 1995]. Models with nearly isotropic lid structures [e.g., *Schlue and Knopoff*, 1977; *Regan and Anderson*, 1984] do not appear to be capable of satisfying the Tonga-Hawaii data.

Models with anisotropy confined to the lid [e.g., *Mitchell and Yu*, 1980] also fail to fit the data (Figure 12), so there must be some anisotropy in the sub-G layer of the LVZ. Our inversion experiments suggest that the average shear anisotropy in this layer must be greater than ~2%. In PA5 the shear anisotropy ratio increases slightly, though insignificantly, across G (from 3.4% to 4.3%), and then decreases linearly to 1.9% at the L discontinuity. While the lack of a resolvable peak in *ScS* reflectivity profile indicates that the *SV* impedance contrast across L is probably less than ~1%, a more substantial (negative) contrast in v_{SH} is allowable. For example, a model with v_{SH} set to a constant value of 4.45 km/s in the sub-G layer fits the data as well as PA5. Such a structure implies a sharp decrease in the Voigt average of the shear velocities at L, however, which is difficult to explain in the context of a peridotitic mantle of constant composition [*Leven et al.*, 1981; *Gaherty and Jordan*, 1995]. For this reason, the L discontinuity in PA5 was constrained to be small.

The explanation of sub-G anisotropy is ambiguous. It could be caused by LPO in olivine [*Ribe*, 1989] or by the preferred orientation of melt-filled pockets [*Schlue and Knopoff*, 1977]; moreover, the alignment of the LPO and/or melt pockets could be induced by paleo-strains that took place near the ridge crest [*Ribe*, 1989, 1992; *Zhang and Karato*, 1995] or by shearing in the asthenosphere due to present-day plate motions [*Montagner and Tanimoto*, 1991]. The plate-motion changes during the long cooling history of the central and western Pacific have been large enough to potentially complicate the depth distribution of azimuthal anisotropy. For example, the seafloor-spreading direction differs by about 40° from the azimuth of the current absolute plate motion where the Tonga-Hawaii corridor crosses the Clipperton fracture zone. There is some seismic evidence for an azimuth variation with depth; the high-frequency Rayleigh-wave propagation in the central and western Pacific as a whole is fastest roughly parallel to the fracture zones [*Nishimura and Forsyth*, 1988], while longer-period Rayleigh waves [*Nishimura and Forsyth*, 1988; *Montagner and Tanimoto*, 1991] and vertical shear-wave splitting [*Farra and Vinnik*, 1994; *Su and Park*, 1994] imply a fast direction roughly parallel to absolute plate motion. The termination of the anisotropy at the L discontinuity in PA5 could correspond to the base of the zone of coherent horizontal deformation (either fossilized or active) or to a change from dislocation-dominated to diffusion-dominated creep within an active shear zone, as suggested by *Karato* [1992].

G Discontinuity

The PA5 shear velocities drop by about 6% across a G discontinuity at 68 ± 4 km. This depth may be an overestimate, because PA5 predicts a value of t_G that is 2.2 s larger than the *ScS* reverberation datum. If the *SV* lid velocity is fixed at the PA5 value of 4.66 km/s, the observed time is fit exactly by z_G = 59 km. However, thinning the lid while still maintaining the fit to the surface waves requires an increase of ~0.15 km/s to both v_{SV} and v_{SH}, driving them to values on the order of 4.8 and 5.0

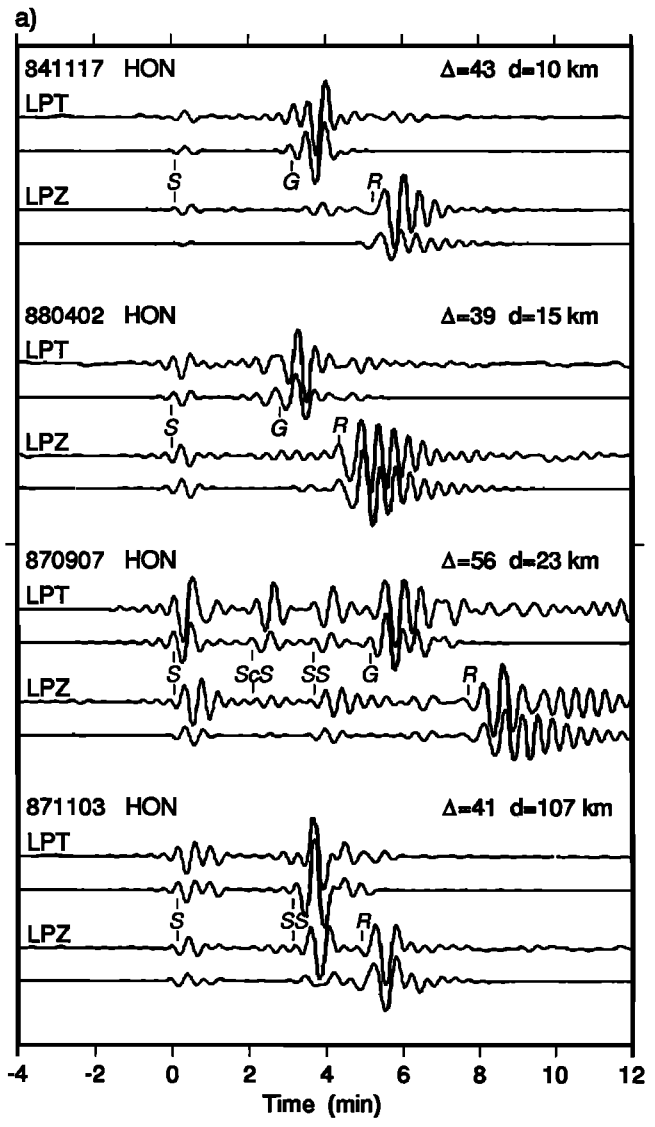

Figure 13a. Comparisons between observed and synthetic seismograms from four representative shallow- and intermediate-focus events. Each event is represented by both tangential- (LPT) and vertical- (LPZ) component seismograms; for each event pair, the top trace is the data, the bottom trace is the synthetic for final model PA5. The traces are aligned (at 0 min) on the *S* wave, with the synthetic seismograms further corrected for an event static, and major phases are labeled. All traces are low-passed with a 45-mHz corner.

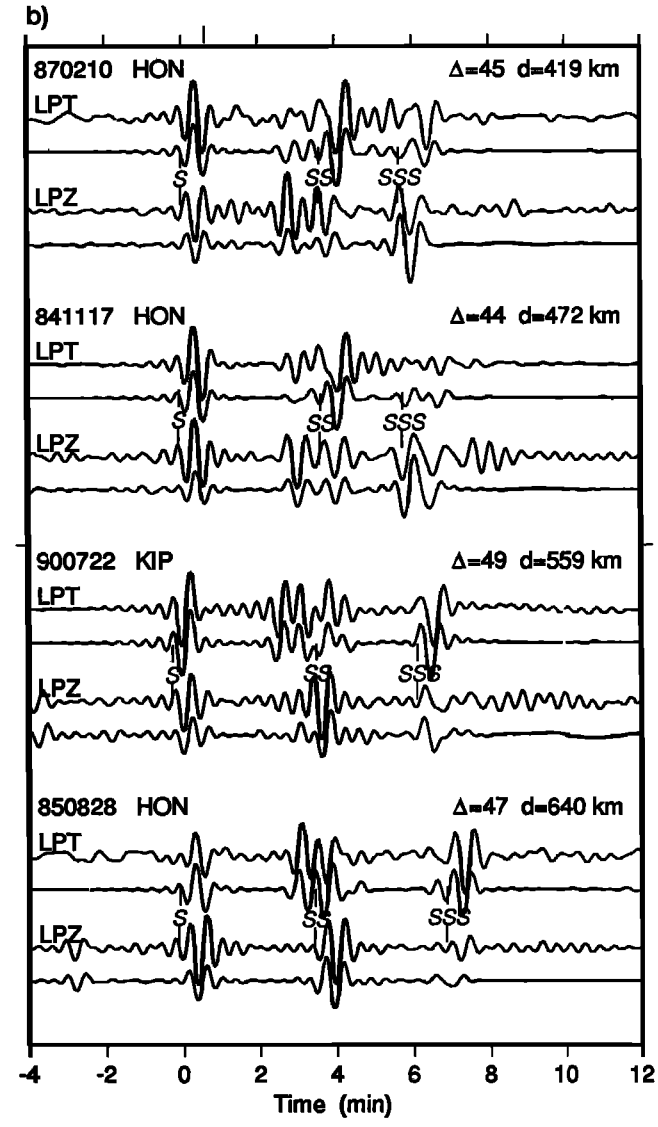

Figure 13b. Same as Figure 13a, except for four representative deep-focus events. The large amplitude phases arriving just prior to *SS* are *sS* and *ScS*. An example of misfit due to poorly modeled *ScS* can be seen near 3 minutes on LPT for 870210 and 841117.

km/s, respectively. Lid velocities of this magnitude are difficult to reconcile with S_n apparent velocities of 4.70-4.80 km/s typically observed for earthquakes in older oceanic regions [*Walker*, 1977] and the values of 4.55-4.75 km/s found in a refraction experiment using a borehole seismometer just east of the Tonga trench [*Shearer and Orcutt*, 1986]. (Although S_n times are usually read from short-period, vertical-component seismograms, the 3-D scattering of these high-frequency waves tends to couple the two quasi-shear waves, so that their travel times are expected to give an average intermediate to the *SH* and *SV* velocities; because they are picked as first arrivals, they may be weighted more heavily towards *SH* [*Gee and Jordan*, 1988].) Since it is possible that the G peak in the reflectivity profile of Figure 2 is biased by an unresolved H discontinuity [*Revenaugh and Jordan*, 1991c], we accepted the t_G misfit.

In any case, the path-average lid velocities for the Tonga-Hawaii corridor are higher and the lid/LVZ transition is shallower than in most previous isotropic models. For example, z_G is about 100 km in PA2 and *Grand and Helmberger*'s [1984b] western-Atlantic model ATL (Figure 14), and a comparable value has been inferred for the central Pacific by *Zhang and Tanimoto* [1993] from their global 3-D model [see also *McNutt*, 1995]. On the other hand, the PA5 estimate of z_G is similar to those found in the radially anisotropic models by *Regan and Anderson* [1984] and *Nishimura and Forsyth* [1989]. It is also consistent with the lid thickness directly beneath Hawaii observed in *S*-to-*P* converted phases [*Bock*, 1991].

Heat-flow and bathymetry data indicate that the thermal boundary layer (TBL) for 100-Ma oceanic plates extends to depths of 100-120 km [*Parsons and Sclater*, 1977; *Stein and*

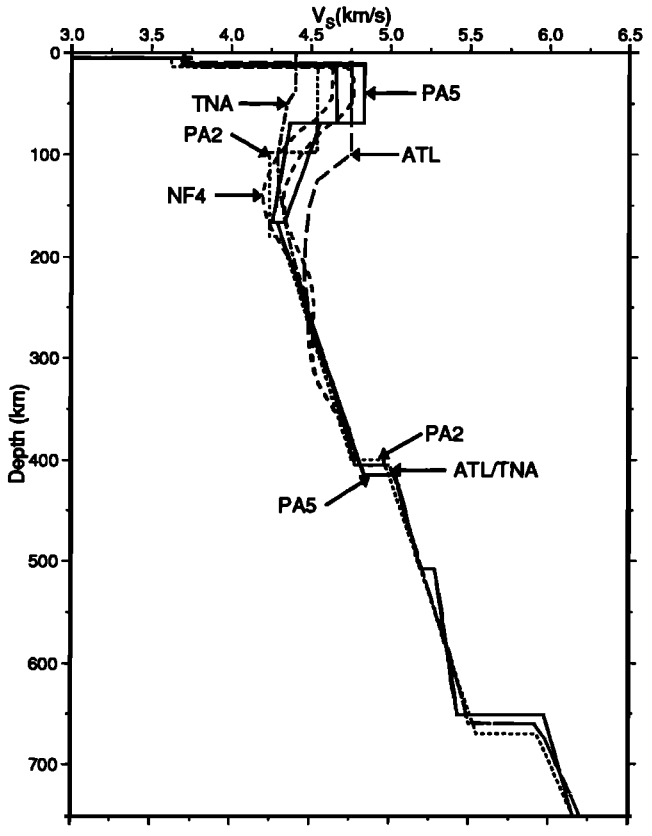

Figure 14. Comparison of PA5 to other oceanic upper-mantle shear-velocity models. PA2 [*Lerner-Lam and Jordan*, 1987] is a Pacific model designed to fit Rayleigh waves. ATL [*Grand and Helmberger*, 1984b] is an *SH* model for the Atlantic. TNA [*Grand and Helmberger*, 1984a] is an *SH* model for tectonic North America, including the northern extent of the East Pacific Rise. The model labeled NF4 is the 52-110 Ma portion from a regionalized anisotropic model of the Pacific [*Nishimura and Forsyth*, 1989]. Note the good agreement among PA5, ATL, TNA, and PA2 on the gradient between 200 and 410 km.

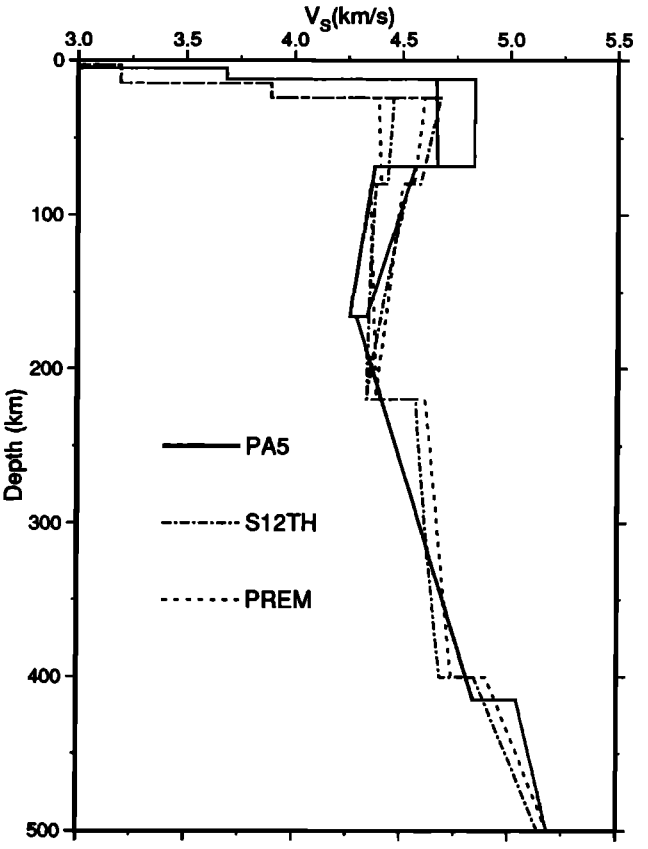

Figure 15. Shear velocities for model PA5, a path-averaged approximation of S12_WM13 [*Su et al.*, 1993] for the Tonga-Hawaii corridor (labeled "S12TH"), and PREM. S12TH is calculated by integrating the S12_WM13 heterogeneity over the path from Tonga/Fiji to Hawaii and applying this mean *S*-velocity perturbation to both v_{SH} and v_{SV} in PREM. For each model, the higher lid/LVZ velocity is v_{SH}, the lower velocity is v_{SV}.

Stein, 1992; *Carlson and Johnson*, 1994; *McNutt*, 1995]. Therefore, in the central Pacific, G is a feature internal to the oceanic TBL rather than defining its base. The existence of a sharp reflectivity peak implies that G must be a relatively narrow transition, with most of the impedance drop occurring over an interval of less than 30 km [*Revenaugh and Jordan*, 1991b]. The data on surface-wave attenuation are consistent with (though do not require) a large drop in Q across this boundary (Figure 2), suggesting that this feature corresponds to an abrupt drop in the solidus temperature with depth. In an isochemical mantle, this decrease could be caused by the release of water owing to the destabilization of hydrated phases like amphibole [cf. *Ringwood*, 1975, Figure 4.7]. However, the amount of water in the normal oceanic upper mantle appears to be small enough, of the order of a few hundred parts per million [*Dixon et al.*, 1988; *Michael*, 1988], to be accommodated in the nominally anhydrous phases such as pyroxene [*Bell and Rossman*, 1992] and olivine [*Bai and Kohlstedt*, 1992], in which case hydrous minerals would not play a significant role in determining the depth dependence of the solidus.

We prefer an alternative scenario in which the decrease in the solidus temperature corresponds to an increase in the total amount of water. A chemical transition of this sort could be the result of the decompression melting at the ridge crest, where the separation of basaltic magma from peridotites is an efficient mechanism for drying out the uppermost mantle [*Hirth and Kohlstedt*, 1996]. In *Hirth and Kohlstedt*'s [1996] model, the water content in olivine increases rapidly below the zone of residual harzburgite, and since water has a substantial effect on the long-term mechanical strength of olivine [e.g., *Karato and Wu*, 1993], this causes a large downward decrease in viscosity. This increase in water will also decrease the seismic velocities [*Karato*, 1995]. In this scenario therefore, G would represent the fossilized lower boundary of the melt separation zone. This hypothesis has the advantage of potentially explaining the peculiar observation of a thicker but slower seismic lid in the Philippine Sea [*Gaherty et al.*, 1995].

High-Gradient Zone

The gradient in shear velocity between the L and 410-km discontinuities is high, $(2.2 \pm 0.2) \times 10^{-3}$ s^{-1}, and well determined by the data. This HGZ appears to be a characteristic feature of oceanic upper mantle. The PA5 velocities in this range nearly coincide with those obtained from 1-D isotropic models of the North Atlantic [*Grand and Helmberger*, 1984a], the East Pacific

Rise [*Grand and Helmberger*, 1984b], and the northwest Pacific [*Lerner-Lam and Jordan*, 1987] (Figure 14). The global 3-D tomographic models that use PREM as a reference, such as S12_WM13 of *Su et al.* [1994], typically have smaller gradients at these depths (Figure 15), and they are consequently less successful in matching the waveforms at higher frequencies (Figure 16).

The high gradient below L excludes the possibility that there can be a significant increase in either the *SV* or *SH* impedance at L, which is consistent with the absence of an L peak in the *SV* reflectivity profile. This implies that there is no distinct base to the LVZ in this depth range, and that the association of L with such an increase [e.g., *Lehmann*, 1959; *Anderson*, 1979; *Hales*, 1991] can be discounted, at least in the upper mantle beneath old ocean basins. From the available data it appears that L is more accentuated beneath continents, where it represents a fairly abrupt transition from an anisotropic zone to a more isotropic region of the upper mantle [*Revenaugh and Jordan*, 1991c; *Gaherty and Jordan*, 1995]. As in the other oceanic models in Figure 14, the low-velocity "channel" in PA5 extends from G all the way to the 410.

In this region of the mantle, the continental cratons typically display higher values and lower gradients in v_S than old ocean basins [*Lerner-Lam and Jordan*, 1983, 1987; *Grand and Helmberger*, 1984b], an inference which supports the hypothesis that the continental cratons are characterized by a very thick (300-400 km), chemically stabilized TBL [*Jordan*, 1975, 1988]. Some authors have questioned this inference on the grounds that the previous seismic studies did not explicitly account for upper-mantle anisotropy [e.g., *Anderson*, 1979; *Karato*, 1992]. However, the shear velocities in *Gaherty and Jordan*'s [1995] 1-D, anisotropic model for Australia (AU3), obtained by an analysis nearly identical to that used here, are fast relative to PA5 down to depths exceeding 300 km, consistent with the thick-TBL hypothesis.

The HGZ may be due in part to the gradual solution of pyroxene into garnet component over a broad depth interval [*Akaogi and Akimoto*, 1977; *Irufine and Ringwood*, 1987], but the much lower gradient in the AU3 continental model suggests that the HGZ is primarily governed by the thermal structure of the convecting oceanic upper mantle. The geotherm $T(z)$ in this convecting region should approximate an adiabat with a gradient of about 0.3 K/km [*Ita and Stixrude*, 1992]. Since the solidus temperature $T_m(z)$ for mantle peridotites has a significantly larger gradient, of the order of 1.0 K/km or greater [*Thompson*, 1992], the homologous temperature T/T_m will decrease by 10% or more over the HGZ. If the mantle adiabat approaches the mantle solidus at the top of the HGZ, then $dv_S/d(T/T_m)$ may be sufficiently large [e.g., *Sato et al.*, 1989] to explain the high shear-velocity gradient.

Transition Zone

The 410 discontinuity in PA5 occurs at 415 ± 3 km, somewhat deeper than that in either ATL or PA2, but nearly identical to the average value of 414 ± 2 km obtained by *Revenaugh and Jordan* [1991b] for the southwest Pacific and Australasia and *Shearer*'s [1993] global average of 413 km. The Δv_S of this discontinuity is 4.1 ± 0.9%, similar to other regional and global seismic models, and its velocity-density ratio, $\Delta v_S/\Delta\rho$ = 1.1 ± 0.3, is consistent with a pyrolite mineralogy [*Weidner*, 1985; *Ita and Stixrude*, 1992]. The 660 discontinuity is shallow (651 ± 4 km) relative to Revenaugh and Jordan's average (660 ± 2 km), but similar to Shearer's (653 km). Compared with most other studies,

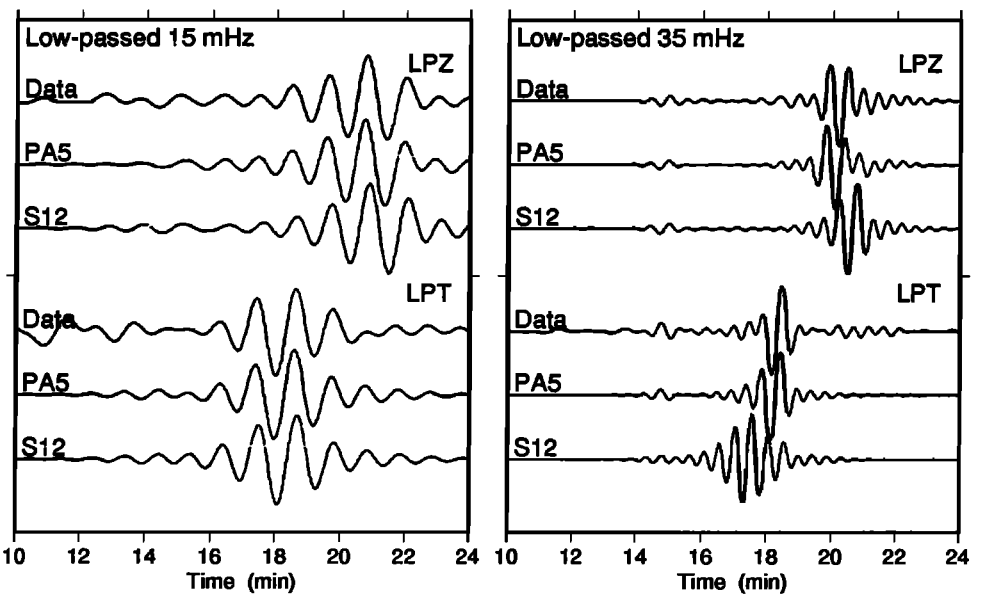

Figure 16. Observed and synthetic seismograms for models PA5 and S12_WM13 for a shallow-focus event. The *S* wave arrives at 14.5 min, G_1 at ~18 min, and R_1 at ~20 min. Vertical-component seismograms are on top, and transverse-component seismograms are on the bottom. Synthetics are aligned on the *S* wave to remove the source static, and the S12_WM13 seismograms are calculated from the spherical harmonic coefficients using the asymptotic perturbation scheme of *Woodhouse and Dziewonski* [1984]. (left) Seismograms low-pass filtered with a corner at 15 mHz. Such data are used in both the S12_WM13 and PA5 analyses, and both models fit the data fairly well. (right) Seismograms low-pass filtered with a corner at 35 mHz. Such data are included in the PA5 inversion, but not that for S12_WM13; PA5 fits the data better.

its shear-wave amplitude is large ($\Delta v_S = 9.9 \pm 1.5\%$). Although PA5 fits the reflectivity datum for 660 (Table 1), $\Delta v_S / \Delta \rho$ for this discontinuity is high (1.5) relative to the values of 0.6-1.0 estimated for isochemical pyrolite models [*Bass and Anderson*, 1984; D. Weidner, personal communication, 1995]. The significance of this discrepancy should be questioned, however, because the GSDF data constraints in this region are weaker than at shallower depths, and this ratio could be biased upward by our parameterization of structural variations below 660 (we tied PA5 to PREM at 801 km, for example).

PA5 includes a 520 discontinuity at 507 ± 10 km, with $\Delta v_S = 1.5 \pm 0.5\%$ and $\Delta \rho = 0.7 \pm 0.5\%$. These combine to give a shear impedance contrast of 1.3%, which is within the error of the *ScS*-reverberation data (2.1 ± 1.5%). The 520 appears to be a global feature [*Shearer*, 1990; *Revenaugh and Jordan*, 1991b] most likely caused by the β–γ transition in $(Mg, Fe)_2SiO_4$, and the velocity and density contrasts that we obtain for this discontinuity are consistent with the available mineralogical data [*Rigden et al.*, 1991; *Bina*, 1991]. However, the width of the β–γ transition is probably at least 30 km [*Akaogi et al.*, 1989], and the exsolution of calcium perovskite may also contribute to this feature [*Gasparik*, 1990; *Bina*, 1991]. Since these effects tend to broaden the transition, modeling it as a sharp discontinuity, as done with the *ScS* reverberation data in recovering the impedance contrast, could underestimate the total impedance contrast of the transition [*Revenaugh and Jordan*, 1991b].

The shear-velocity gradients in the transition zone are lower in PA5 than in PREM and most other global seismic models (except below 600 km, where PREM has a slope break to a low gradient that is similar to PA5). The gradient between the 410 and the 520 is very close to ATL, but between the 520 and the 660 it is lower (Figure 14), owing to the jump at 520 and the larger contrast across the 660. The lower gradients bring the seismically determined shear velocities more in line with the predictions for a pyrolitic composition [*Weidner*, 1985; *Rigden et al.*, 1991].

Conclusions

PA5 results from a first attempt to satisfy both *ScS* reverberation data on mantle discontinuities and frequency-dependent travel times of *PSV*- and *SH*-polarized phases that are sensitive to velocity gradients and anisotropy. The data have been collected using a consistent methodology from a common source-receiver array that samples old oceanic lithosphere in a corridor traversing the central Pacific. We have shown that these data can be successfully modeled in conjunction with attenuation data and mineralogical constraints on bulk sound velocity and density to obtain a complete spherically symmetric, radially anisotropic structure for this path.

The vertical resolution of mantle layering that results from this procedure is superior to previous studies. In Figure 15, the PA5 upper mantle is compared with the corresponding path average of the aspherical global tomographic model S12_WM13, and in Figure 16, synthetic seismograms calculated from these models are compared with data for vertical and transverse components of ground motion. At low frequencies (~15 mHz), both models yield good fits to these observations, but at higher frequencies (~35 mHz), the fit of the tomographic model is poor. While the incorporation of higher-frequency data into the aspherical models can be expected to improve the fits in the near future [e.g., *Ekström and Dziewonski*, 1995], it will be some time before tomography can achieve this level of vertical resolution.

Acknowledgments. We thank the Harvard and IRIS data centers for their assistance in collecting digital seismograms, and T. Grove, G. Hirth, S. Karato, M. Kato, and D. Weidner for useful discussions regarding mantle mineralogy. Thorough reviews by J. Park and P. Shearer improved our discussion of anisotropy. All figures were generated using the GMT software freely distributed by *Wessel and Smith* [1991]. This research was supported by Air Force Office of Scientific Research under grants F49620-92-J-0404 and F49620-95-1-0051, and the National Science Foundation under grant EAR-94-18439.

References

Akaogi, M., and S. Akimoto, Pyroxene-garnet solid solution equilibria in the system $Mg_4Si_4O_{12}$-$Mg_3Al_2Si_3O_{12}$ and $Fe_4Si_4O_{12}$-$Fe_3Al_2Si_3O_{12}$ at pressures and temperatures, *Phys. Earth Planet. Inter., 15*, 90-106, 1977.

Akaogi, M., E. Ito, and A. Navrotsky, Olivine-modified spinel-spinel transitions in the system Mg_2SiO_4-Fe_2SiO_4: Calorimetric measurements, thermochemical calculation, and geophysical application, *J. Geophys. Res., 94*, 15,671-15,685, 1989.

Anderson, D.L., Elastic wave propagation in layered anisotropic media, *J. Geophys. Res., 66*, 2953-2963, 1961.

Anderson, D.L., The deep structure of continents, *J. Geophys. Res., 84*, 7555-7560, 1979.

Anderson, D.L., and A.M. Dziewonski, Upper mantle anisotropy: Evidence from free oscillations, *Geophys. J. R. Astron. Soc., 69*, 383-404, 1982.

Bai, Q. and D.L. Kohlstedt, Substantial hydrogen solubility in olivine and implications for water storage in the mantle, *Nature, 357*, 672-674, 1992.

Bass, J.D., and D.L. Anderson, Composition of the upper mantle: Geophysical tests of two petrological models, *Geophys. Res. Lett., 11*, 237-240, 1984.

Bell, D.R., and G.R. Rossman, Water in Earth's mantle: The role of nominally anhydrous minerals, *Science, 255*, 1391-1397, 1992.

Bina, C.R., Mantle discontinuities, *U.S. Natl. Rep. Int. Union Geod. Geophys. 1987-1990, Rev. Geophys., 29*, 783-793, 1991.

Bock, G., Long-period *S* to *P* converted waves and the onset of partial melting beneath Oahu, Hawaii, *Geophys. Res. Lett., 18*, 869-872, 1991.

Cara, M., and J.J. Lévêque, Anisotropy of the asthenosphere: the higher mode data of the Pacific revisited, *Geophys. Res. Lett., 15*, 205-208, 1988.

Carlson, R.L., and H.P. Johnson, On modeling the thermal evolution of the oceanic upper mantle: An assessment of the cooling plate model, *J. Geophys. Res., 99*, 3201-3214, 1994.

Christensen, N.I., The magnitude, symmetry, and origin of upper mantle anisotropy based on fabric analyses of ultramafic tectonites, *Geophys. J. R. Astron. Soc., 76*, 89-111, 1984.

Dixon, J.E., E. Stolper, and J.R. Delaney, Infrared spectroscopic measurements of CO_2 and H_2O in Juan de Fuca ridge basaltic glasses, *Earth Planet. Sci. Lett., 90*, 87-104, 1988.

Dziewonski, A.M. and D.L. Anderson, Preliminary reference Earth model, *Phys. Earth Planet. Inter., 25*, 297-356, 1981.

Dziewonski, A. M., J. Mills, and S. Bloch, Residual dispersion measurement - A new method of surface-wave analysis, *Bull. Seismol. Soc. Am., 62*, 129-139, 1972.

Dziewonski, A. M., T.-A. Chou, and J. H. Woodhouse, Determination of earthquake source parameters from waveform data for studies of global and regional seismicity, *J. Geophys. Res., 86*, 2825-2852, 1981.

Ekström, G. and A.M. Dziewonski, Improved models of upper mantle S velocity structure (abstract), *Eos Trans. AGU, 76* (46), Fall Meet. Suppl., F421, 1995.

Estey, L.H., and B.J. Douglas, Upper mantle anisotropy: A preliminary model, *J. Geophys. Res., 91*, 11,393-11,406, 1986.

Farra, V., and L. Vinnik, Shear-wave splitting in the mantle of the Pacific, *Geophys. J. Int., 119*, 195-218, 1994.

Forsyth, D.W., The early structural evolution and anisotropy of the oceanic upper mantle, *Geophys. J. R. Astron. Soc., 43*, 103-162, 1975a.

Forsyth, D.W., A new method for the analysis of multi-mode surface-wave dispersion: Application to Love-wave propagation in the east Pacific, *Bull. Seismol. Soc. Am., 65*, 323-342, 1975b.

Gaherty, J.B., Structure and anisotropy of the upper mantle, Ph.D. thesis, Mass. Inst. Tech., Cambridge, 1995.

Gaherty, J.B., and T.H. Jordan, Lehmann discontinuity as the base of an anisotropic layer beneath continents, *Science*, *268*, 1468-1471, 1995.

Gaherty, J.B., M. Kato, and T.H. Jordan, Plate structure and seismic anisotropy in the western Pacific (abstract), *Eos Trans. AGU*, *76* (46), Fall Meet. Suppl., F421, 1995.

Garnero, E.J. and D.V. Helmberger, Seismic detection of a thin laterally varying boundary layer at the base of the mantle beneath the central Pacific, *Geophys. Res. Lett.*, *23*, 977-980, 1996.

Gasparik, T., Phase relations in the transition zone, *J. Geophys. Res.*, *95*, 15,751-15,769, 1990.

Gee, L.S., and T.H. Jordan, Polarization anisotropy and fine-scale structure of the Eurasian upper mantle, *Geophys. Res. Lett.*, *15*, 824-827, 1988.

Gee, L.S., and T. H. Jordan, Generalized seismological data functionals, *Geophys. J. Int.*, *111*, 363-390, 1992.

Grand, S.P., and D.V. Helmberger, Upper mantle shear structure of North America, *Geophys. J. R. Astron. Soc.*, *76*, 399-438, 1984a.

Grand, S.P., and D.V. Helmberger, Upper mantle shear structure beneath the northwest Atlantic Ocean, *J. Geophys. Res.*, *89*, 11,465-11,475, 1984b.

Gripp, A.E., and R.G. Gordon, Current plate velocities relative to the hotspots incorporating the NUVEL-1 global plate motion model, *Geophys. Res. Lett.*, *17*, 1109-1112, 1990.

Hales, A.L., Upper mantle models and the thickness of continental lithosphere, *Geophys. J. Int. 105*, 355-363, 1991.

Herrin, E., and T. Goforth, Phase-matched filters: application to the study of Rayleigh waves, *Bull. Seismol. Soc. Am.*, *67*, 1259-1275, 1977.

Hess, H., Seismic anisotropy of the uppermost mantle under oceans, *Nature*, *203*, 629, 1964.

Hirth, G., and D.L. Kohlstedt, Water in the oceanic upper mantle: Implications for rheology, melt extraction, and the evolution of the lithosphere, *Earth. Planet. Sci. Lett.*, in press, 1996.

Irufine, T., and A.E. Ringwood, Phase transformations in primitive MORB and pyrolite compositions to 25 GPa and some geophysical implications, in *High-Pressure Research in Mineral Physics, Geophys. Monogr. Ser.*, vol. 39 (Mineral Physics, vol. 2), edited by M.H. Manghnani and Y. Syono, pp. 231-242, AGU, Washington, D.C., 1987.

Ita, J., and L. Stixrude, Petrology, elasticity, and composition of the mantle transition zone, *J. Geophys. Res.*, *97*, 6849-6866, 1992.

Jordan, T.H., The continental tectosphere, *Rev. Geophys.*, *13*, 1-12, 1975.

Jordan, T.H., Structure and formation of the continental tectosphere, *J. Petrol. Special Lithosphere Issue*, 11-37, 1988.

Jordan, T. H., and J. B. Gaherty, Stochastic modeling of small-scale, anisotropic structures in the continental upper mantle, paper presented at 17th Annual Seismic Research Symposium, Phillips Lab., Bedford, Mass., 433-451, 1995.

Joseph, D., B. Taylor, A.N. Shor, and T. Yamazaki, The Nova-Canton trough and the late Cretaceous evolution of the central Pacific, in *The Mesozoic Pacific: Geology, Tectonics, and Volcanism, Geophys. Monogr. Ser.*, vol. 77, edited by M. Pringle, W. Sager, W Sliter, and S. Stein, pp. 171-185, AGU, Washington, D.C., 1987.

Karato, S.-I., On the Lehmann discontinuity, *Geophys. Res. Lett.*, *19*, 2255-2258, 1992.

Karato, S.-I., Effects of water on seismic wave velocities in the upper mantle, *Proc. Jpn Acad., Ser. B*, *71*, 61-66, 1995.

Karato, S.-I., and P. Wu, Rheology of the upper mantle: A synthesis, *Science*, *260*, 771-778, 1993.

Katzman, R., L. Zhao, J.B. Gaherty, and T.H. Jordan, Teleseismic tomography using generalized seismological data functionals and *ScS* reverberations (abstract), *Eos Trans. AGU*, *77* (22), West. Pac. Geophys. Meet. Suppl., 85, 1996.

Kawasaki, I., and F. Kon'no, Azimuthal anisotropy of surface waves and the possible type of the seismic anisotropy due to preferred orientation of olivine in the uppermost mantle beneath the Pacific Ocean, *J. Phys. Earth*, *32*, 229-244, 1984.

Kovach, R. L., and D. L. Anderson, Higher modes surface waves and their bearing on the structure of the Earth's mantle, *Bull. Seismol. Soc. Am.*, *54*, 161-182, 1964.

Leeds, A.R., L. Knopoff, and E.G. Kausel, Variations in upper mantle structure under the Pacific ocean, *Science*, *186*, 141-143, 1974.

Lehmann, I., Velocities of longitudinal waves in the upper part of the Earth's mantle, *Ann. Geophys.*, *15*, 93-118, 1959.

Lerner-Lam, A.L., and T.H. Jordan, Earth structure from fundamental and higher-mode waveform analysis, *Geophys. J. R. Astron. Soc.*, *75*, 759-797, 1983.

Lerner-Lam, A.L. and T.H. Jordan, How thick are the continents?, *J. Geophys. Res.*, *92*, 14007-14026, 1987.

Leven, J.H., I. Jackson, and A.E. Ringwood, Upper mantle seismic anisotropy and lithospheric decoupling, *Nature*, *289*, 234-239, 1981.

Lévêque, J.J. and M. Cara, Long-period Love wave overtone data in North America and the Pacific Ocean: New evidence for upper mantle anisotropy, *Phys. Earth Planet. Inter.*, *33*, 164-179, 1983.

Liu, H.-P., D.L. Anderson, and H. Kanamori, Velocity dispersion due to anelasticity: Implications for seismology and mantle composition, *Geophys. J.*, *47*, 41-58, 1976.

Ludwig, W.J. and R.E. Houtz, Isopach map of sediments in the Pacific ocean basin and marginal sea basins, Am. Assoc. Petrol. Geol., Tulsa, Okla., 1979.

Luo, Y. and G.T. Schuster, Wave equation traveltime inversion, *Geophysics*, *56*, 645-653, 1991.

Maupin, V., Partial derivatives of surface-wave phase velocities for flat anisotropic models, *Geophys. J. R. Astron. Soc.*, *83*, 379-398, 1985.

McEvilly, T.V., Central US crust-upper mantle structure from Love and Rayleigh wave phase velocity inversion, *Bull. Seismol.. Soc. Am.*, *54*, 1997-2015, 1964.

McNutt, M.K., Marine geodynamics: Depth-age revisited, *U.S. Natl. Rep. Int. Union Geod. Geophys. 1991-1994, Rev. Geophys.*, *33*., 413-418, 1995.

McNutt, M.K., and K.M. Fischer, The south Pacific Superswell, in *Seamounts, Islands, and Atolls, Geophys. Monogr. Ser.*, vol. 43, edited by B.H. Keating, P.Fryer, R. Batiza, G.W. Boehlert, pp. 969-975, AGU, Washington, D.C., 1987.

Menard, H.W., Extension of the northeastern Pacific fracture zones, *Science*, *155*, 72-74, 1967.

Menard, H.W., Darwin reprise, *J. Geophys. Res.*, *89*, 9960-9968, 1984.

Michael, P.J., The concentration, behavior, and storage of H_2O in the suboceanic mantle: Implications for mantle metasomatism, *Geochim. Cosmochim. Acta*, *52*, 555-566, 1988.

Mitchell, B.J., and G. Yu, Surface wave dispersion, regionalized velocity models, and anisotropy of the Pacific crust and upper mantle, *Geophys. J. R. Astron. Soc.*, *63*, 497-514, 1980.

Montagner, J.-P., and D.L. Anderson, Petrological constraints on seismic anisotropy, *Phys. Earth Planet. Inter.*, *54*, 82-105, 1989.

Montagner, J.-P., and T. Tanimoto, Global upper-mantle tomography of seismic velocities and anisotropy, *J. Geophys. Res.*, *96*, 20,337-20,351, 1991.

Mueller, R.D., Roest, W.R., Royer, J.-Y., Gahagan, L.M., and Sclater, J.G., A digital age map of the ocean floor, *SIO Reference Series 93-30*, 1993.

Nataf, H.-C., I. Nakanishi, and D.L. Anderson, Measurements of mantle-wave velocities and inversion for lateral heterogeneities and anisotropy, 3., Inversion, *J. Geophys. Res.*, *91*, 7261-7307, 1986.

Nicolas, A., and N.I. Christensen, Formation of anisotropy in upper mantle peridotites: A review, in *Composition, Structure, and Dynamics of Lithosphere-Asthenosphere System, Geodyn. Ser.*, vol. 16, edited by K. Fuchs and C. Froidevaux, pp. 111-123, AGU, Washington, D.C., 1987.

Nishimura, C.E., and D.W. Forsyth, Rayleigh wave phase velocities in the Pacific with implications for azimuthal anisotropy and lateral heterogeneities, *Geophys. J.*, *94*, 479-501, 1988.

Nishimura, C.E., and D.W. Forsyth, The anisotropic structure of the upper mantle in the Pacific, *Geophys. J.*, *96*, 203-229, 1989.

Nolet, G., Higher Rayleigh modes in western Europe, *Geophys. Res. Lett.*, *2*, 60-62, 1975.

Nolet, G., S.P. Grand, and B.L.N. Kennett, Seismic heterogeneity in the upper mantle, *J. Geophys. Res.*, *99*, 23,753-23,766, 1994.

Parsons, B., and J. Sclater, An analysis of the variation of ocean bathymetry and heat flow with age, *J. Geophys. Res.*, *82*, 803-827, 1977.

Press, F., Rigidity of the earth's core, *Science*, *124*, 1204, 1956.

Regan, J., and D.L. Anderson, Anisotropic models of the upper mantle, *Phys. Earth Planet. Int.*, *35*, 227-263, 1984.

Revenaugh, J.S., The nature of mantle layering from first-order reverberations, Ph.D thesis, Mass. Inst. Technol., Cambridge, 1989.

Revenaugh, J.S., and T. H. Jordan, Observations of first-order mantle reverberations, *Bull. Seismol. Soc. Am.*, *77*, 1704-1717, 1987.

Revenaugh, J.S., and T. H. Jordan, A study of mantle layering beneath the western Pacific, *J. Geophys. Res.*, *94*, 5787-5813, 1989.

Revenaugh, J.S., and T.H. Jordan, Mantle layering from *ScS* reverberations, 1, waveform inversion of zeroth-order reverberations, *J. Geophys. Res.*, *96*, 19,749-19,762, 1991a.

Revenaugh, J.S., and T.H. Jordan, Mantle layering from *ScS* reverberations, 2, The transition zone, *J. Geophys. Res., 96,* 19,763-19,780, 1991b.

Revenaugh, J.S., and T.H. Jordan, Mantle layering from *ScS* reverberations, 3, The upper mantle, *J. Geophys. Res., 96,* 19,781-19,810, 1991c.

Revenaugh, J.S., and T.H. Jordan, Mantle layering from *ScS* reverberations, 4, The lower mantle and the core-mantle boundary, *J. Geophys. Res., 96,* 19,811-19,824, 1991d.

Ribe, N.M., Seismic anisotropy and mantle flow, *J. Geophys. Res., 94,* 4213-4223, 1989.

Ribe, N.M., On the relation between seismic anisotropy and finite strain, *J. Geophys. Res., 97,* 8737-8747, 1992.

Rigden, S.M., G.D. Gwanmesia, J.D. Fitzgerald, I. Jackson, and R.C. Lieberman, Spinel elasticity and the seismic structure of the transition zone of the mantle, *Nature, 345,* 143-145, 1991.

Ringwood, A.E., *Composition and Petrology of the Earth's Mantle,* 604 pp., McGraw-Hill, New York, 1975.

Sato, H., I.S. Sacks, and T. Murase, The use of laboratory velocity data for estimating temperature and partial melt fraction in the low-velocity zone: Comparison with heat flow and electrical conductivity studies, *J. Geophys. Res., 94,* 5689-5704, 1989.

Schlue, J.W. and L. Knopoff, Shear-wave polarization anisotropy in the Pacific basin, *Geophys. J. R. Astron. Soc., 49,* 145-165, 1977.

Shearer, P.M., Seismic imaging of upper mantle structure with new evidence for a 520-km discontinuity, *Nature, 344,* 121-126, 1990.

Shearer, P.M., Global mapping of upper mantle reflectors from long-period *SS* precursors, *Geophys. J. Int., 115,* 878-904, 1993.

Shearer, P.M. and J.A. Orcutt, Compressional and shear wave anisotropy in the oceanic lithosphere -- The Ngendei seismic refraction experiment, *Geophys. J. R. Astron. Soc, 87,* 967-1003, 1986.

Sipkin, S.A., and T.H. Jordan, Frequency dependence of Q_{ScS}, *Bull. Seismol. Soc. Am., 69,* 1055-1079, 1979.

Sipkin, S.A., and T.H. Jordan, Multiple *ScS* travel times in the western Pacific: Implications for mantle heterogeneity, *J. Geophys. Res., 85,* 853-861, 1980a.

Sipkin, S.A., and T.H. Jordan, Regional variation of Q_{ScS}, *Bull. Seismol. Soc. Am., 70,* 1071-1102, 1980b.

Stein, C.A., and S. Stein, A model for the global variation in oceanic depth and heat flow with lithospheric age, *Nature, 359,* 123-129, 1992.

Su, L., and J. Park, Anisotropy and the splitting of *PS* waves, *Phys. Earth Planet. Inter., 86,* 263-276, 1994.

Su, W.-J., R.L. Woodward, and A.M. Dziewonski, Degree-12 model of shear velocity heterogeneity in the mantle, *J. Geophys. Res., 99,* 6945-6980, 1994.

Suetsugu, D., and I. Nakanishi, Regional and azimuthal dependence of phase velocities of mantle Rayleigh waves in the Pacific Ocean, *Phys. Earth Planet. Inter., 47,* 230-245, 1987.

Tarantola, A., *Inverse Problem Theory,* 613 pp., Elsevier, New York, 1987.

Tarantola, A., and B. Valette, Generalized nonlinear inverse problems solved using the least squares criterion, *Rev. Geophys., 20,* 219-232, 1982.

Thatcher, W., and J. N. Brune, Higher mode interference and observed anomalous apparent Love wave phase velocities, *J. Geophys. Res., 74,* 6603-6611, 1969.

Thompson, A.B., Water in the Earth's upper mantle, *Nature, 358,* 295-302, 1992.

Vidale, J.E., and H.M. Benz, Upper-mantle seismic discontinuities and the thermal structure of subduction zones, *Nature, 356,* 678-683, 1992.

Walker, D.A., High-frequency *Pn* and *Sn* phases recorded in the western Pacific, *J. Geophys. Res., 82,* 3350-3360, 1977.

Weidner, D., A mineral physics test of a pyrolite mantle, *Geophys. Res. Lett, 12,* 417-420, 1985.

Wessel, P., and W.H.F. Smith, Free software helps map and display data, *Eos Trans AGU, 72,* 441, 445-446, 1991.

Woodhouse, J.H. and A.M. Dziewonski, Mapping the upper mantle: Three-dimensional modeling of earth structure by inversion of seismic waveforms, *J. Geophys. Res., 89,* 5953-5986, 1984.

Yu, Y., and J. Park, Hunting for azimuthal anisotropy beneath the Pacific Ocean region, *J. Geophys. Res., 99,* 15,399-15,421, 1994.

Zhang, S., and S.-I. Karato, Lattice preferred orientation of olivine in simple shear deformation and the flow geometry of the upper mantle of the Earth, *Nature, 375,* 774-777, 1995.

Zhang, Y.-S., and T. Tanimoto, High-resolution global upper mantle structure and plate tectonics, *J. Geophys. Res., 98,* 9793-9823, 1993.

Zielhuis, A., and G. Nolet, Shear wave velocity variations in the upper mantle beneath central Europe, *Geophys. J. Int., 117,* 695-715, 1994.

J.B. Gaherty and T.H. Jordan, Massachusetts Institute of Technology, Department of Earth, Atmospheric, and Planetary Sciences, Rm. 54-512, Cambridge, MA 02139. (e-mail: gaherty@quake.mit.edu; thj@mit.edu)

L.S. Gee, Seismographic Station, ESB 475, University of California, Berkeley, CA 94720. (e-mail: lind@seismo.berkeley.edu)

(Received January 17, 1996; revised May 24, 1996;
accepted June 4, 1996.)